

Zirconia-supported Pt, Pd, Rh, Ru and Ni Catalysts in the Hydrotreatment of Fatty Amides and Amines

Emma Verkama^{1*}, Sylvia Albersberger², Kristoffer Meinander³, Marja Tiitta^{2†}, Reetta Karinen¹, Riikka L. Puurunen¹

¹Department of Chemical and Metallurgical Engineering, School of Chemical Engineering, Aalto University, P.O. Box 16100, 00076 Aalto, Finland

²Neste Corporation, P.O. Box 310, 06101 Porvoo, Finland

³Department of Bioproducts and Biosystems, School of Chemical Engineering, Aalto University, P.O. Box 16300, 00076 Aalto, Finland

† Present address: Hamari, Finland

* Corresponding author:

Email: emma.verkama@aalto.fi

Abstract

Active catalysts for simultaneous hydrodeoxygenation (HDO) and hydrodenitrogenation (HDN) enable the production of fuels from renewable feedstocks. In this work, zirconia-supported nickel, ruthenium, rhodium, palladium and platinum catalysts were evaluated in the HDO and HDN of *n*-hexadecanamide (C16 amide). The HDN of 1-hexadecylamine (C16 amine) was studied separately to assess the HDN activity and preference between C–C and C–N bond cleavage routes without the interference of HDO. The differences in the catalytic activity were mainly attributed to the metal identity. Pt/ZrO₂ and Ru/ZrO₂ exhibited the highest activity towards the conversion of both model compounds. The C16 amide was converted more efficiently than the C16 amine over the studied catalysts, and a high HDO activity did not translate to a high activity in HDN, which was particularly evident in the case of Rh/ZrO₂. The active metal strongly influenced the preferred reaction routes, as observed from differences in the yields of C15 and C16 *n*-paraffins and C32 condensation products. Ni/ZrO₂ and Pd/ZrO₂ exhibited the lowest activity and paraffin selectivity in the hydrotreatment of both model compounds. Ru/ZrO₂ and Rh/ZrO₂ favored the formation of *n*-pentadecane from both the C16 amine and C16 amide, whereas Pt/ZrO₂ produced *n*-hexadecane and high intermediate yields of the C32 condensation products.

Keywords: hydrodenitrogenation, hydrodeoxygenation, amide, amine, noble metal catalyst

1. Introduction

Renewable fuels enable mitigating the CO₂ emissions of the heavy-duty transport sector and the aviation industry. Major research efforts have consequently been devoted to the hydrotreatment of biobased feedstocks to renewable fuels, with a focus on hydrodeoxygenation (HDO), due to the significant oxygen content of biomass.^{1–8} Some renewable feedstocks, such as animal fats and biocrudes obtained via hydrothermal liquefaction (HTL) of algae and sewage sludge, contain nitrogen in addition to oxygen.^{9–14} Reducing the nitrogen content of such feedstocks via hydrodenitrogenation (HDN) is important, in parallel with HDO, as nitrogen-containing compounds poison catalysts in downstream processing units and negatively impact the fuel stability.¹⁵ While a complete oxygen removal can be obtained in the hydrotreatment of HTL biocrudes, HDN has been found to be more challenging, with the nitrogen removal often ranging between 50 and 80%.^{16–19} There is, thus, a need to develop catalysts that are active for both HDO and HDN. Nevertheless, research on the HDN and HDO of molecules which contain both oxygen and nitrogen is limited,^{20,21} despite the abundance of, e.g., fatty amides in renewable feedstocks.

Supported noble metal catalysts activate hydrogen in relatively mild conditions and are highly active for HDO reactions, especially via decarbonylation and decarboxylation routes.^{5,22,23} Noble metal catalysts also exhibit activity towards C–N bond hydrogenolysis and are therefore an alternative to commercially used transition metal sulfide catalysts for the hydrotreatment of renewable, sulfur-free feedstocks.^{24–26} The HDO and HDN of *n*-hexadecanamide (C₁₆ amide, C₁₆H₃₃NO) to *n*-paraffins was recently studied on a series of supported Pt catalysts by Verkama et al.²⁷ The Lewis acid properties of the support markedly influenced the HDO activity and the selectivity towards the initial conversion route, but the HDN of the nitrogen-containing intermediate products and significant formation of secondary amines and amides limited the overall activity of the catalysts.²⁷ An inhibition of HDN by preferential HDO and condensation product formation has similarly been observed in the co-hydrotreatment of palmitic acid and 1-tetradecylamine over Pt/ZrO₂.²⁸

In the hydrotreatment of fatty amides, the active metal can be expected to markedly influence the conversion of the amine intermediates.^{25,29–33} The activity and selectivity between HDN and condensation of alkyl amines strongly depends on the active metal, which suggests that an appropriately chosen active metal could enhance the paraffin yield and mitigate the formation of condensation products.^{25,29–32} For

example, Rh has been found to favor the formation of hydrocarbons in the hydrotreatment of methylamine, while secondary and tertiary amines readily are formed on Pd.^{25,29–32} The metal identity also influences the activity and selectivity for the HDO of fatty acids and alcohols, i.e., the oxygen-containing compounds that are formed as intermediate products in the hydrotreatment of amides.^{25,34} Here, Ru, Rh, Pd and Ni typically favor decarbonylation and decarboxylation routes, whereas Pt may favor C–O bond hydrogenolysis pathways, particularly if paired with a Lewis acidic support.^{5,22,23,34–37} Considering the impact of the metal identity on the activity for HDN and HDO individually, it is of interest to investigate the effect of the active metal in the hydrotreatment of molecules that contain both oxygen and nitrogen.^{27,28}

In this work, ZrO₂-supported Pt, Pd, Rh, Ru and Ni catalysts were studied in the hydrotreatment of the C16 amide and 1-hexadecylamine (C16 amine, C₁₆H₃₅N). The C16 amide was chosen as a model compound due to the presence of fatty amides in various renewable feedstocks, while the C16 amine was used to assess the HDN activity of the catalysts without the interference of simultaneous HDO.^{9–11,24,38} The purpose of this work was to describe the impact of the active metal on the activity, selectivity and reaction routes in the hydrotreatment of fatty amides and amines, which to the best of our knowledge, has not been addressed before.

2. Experimental

2.1 Materials. Monoclinic zirconia (ZrO₂) from Saint-Gobain Norpro (SZ 31164) was used as the catalyst support. The metal precursors were platinum(IV) nitrate solution (15 wt. % Pt), palladium(II) nitrate solution (12-16 wt. % Pd) and ruthenium(III) nitrosyl nitrate (31.78 wt. % Ru) from Alfa Aesar, as well as rhodium(III) nitrate solution (10 wt. % Rh) and nickel(II) nitrate hexahydrate (99.999% trace metals basis) from Aldrich.

For the reactor experiments and calibrations, the following chemicals were used: *n*-hexadecanamide (>95%, Tokyo Chemical Industry), 1-hexadecylamine (>95%, Tokyo Chemical Industry), *n*-pentadecane (>99%, Aldrich), *n*-hexadecane (>99%, Sigma Aldrich), *n*-hexadecanal (>97%, Tokyo Chemical Industry), 1-hexadecanol (96%, Acros Organics), palmitic acid (>98%, Riedel de Haën), *n*-pentadecanonitrile (>95%, Tokyo Chemical Industry), *n*-heptadecanonitrile (>95%, Tokyo Chemical Industry), palmityl palmitate (>99%, Sigma Aldrich), decalin (decahydronaphthalene, anhydrous, mixture of cis and trans, >99%, Sigma Aldrich), *n*-dodecane (>99%, Merck) and 2-propanol (>99%, Riedel de Haën). The pyridine used for acid site characterization was obtained from Sigma Aldrich (anhydrous, 99.8%). The chemicals were used without further purification.

The hydrogen (99.995%) that was used in the reactor experiments and the nitrogen (99.999%), helium (99.999%), 2 vol. % H₂/Ar gas mixture (99.999%/99.999%) and 10 vol. % CO₂/He (99.999%/99.999%) gas mixture which were used for catalyst characterization, were purchased from Oy AGA Ab. The 10 vol. % CO/He gas mixture (99.999%/99.999%) was from Woikoski, and the helium (99.999%) and synthetic air (99.999%) used in the pyridine FTIR measurements were from Linde. The gases used for the product analysis; synthetic air (99.999%), helium (99.999%), hydrogen (99.999%), argon (99.999%) and oxygen (99.999%) were from Oy AGA Ab and Woikoski.

2.2 Catalyst Preparation. The catalysts were prepared with a vacuum impregnation method using a small excess of impregnation solution, targeting a 1 wt. % active metal loading. The ZrO₂-support was first crushed and sieved to a particle size of 0.25-0.42 mm, and calcined in ambient air at 600 °C in a static muffle furnace for 10 h. The impregnation was done as described previously.²⁸ The catalysts were calcined in a flow through calcination oven under a 100 ml/min flow of synthetic air. The Ru, Rh, Pd and Ni catalysts were calcined at 450 °C for 2 h using a 1 °C/min heating ramp, whereas the Pt catalyst was calcined at 450 °C for 1 h using a 2 °C/min heating ramp.

2.3 Catalyst Characterization. Isothermal N₂-physisorption measurements were carried out at -196 °C for 200 mg samples of the calcined catalysts and the ZrO₂ support, using a Surfer equipment from Thermo Scientific. Liquid nitrogen was used as a coolant. Prior to analysis, the samples were degassed in vacuum at 350 °C for 180 min, using a 5 °C/min heating rate, in order to remove moisture and other adsorbed compounds. A dead volume calibration was carried out with He after every measurement. The Brunauer-Emmett-Teller (BET) method was used to calculate the specific surface area S_{BET} (m²/g) of each sample from the adsorption isotherm, while the Barrett-Joyner-Halenda (BJH) method was used for calculating the pore size distribution, mean pore diameter d_{pore} , (nm) and pore volume V_{pore} (cm³/g) from the desorption branch.^{39,40}

The active metal loading (wt. %) was measured semi-quantitatively with X-ray fluorescence (XRF). The measurements were conducted with a wavelength dispersive PANalytical Axios mAx equipment. Approximately 200 mg samples of the calcined catalysts were ground for the analysis and measured as loose powders in He, using Chemplex 1330-SE sample cups covered with a 3.6 μm mylar film.

The crystallographic phase of the catalysts was identified with X-ray diffraction (XRD) measurements, using a PANalytical X'Pert PRO MPD Alpha-1 X-ray diffractometer, with Cu Kα1 radiation (45 kV, 40 mA). The 2θ scanning range was from 5° to 100°, and a step size of 0.026° was used. The analysis was done for ground samples of the calcined catalysts. The HighScore software was used for phase identification (ICDD PDF-4+ 2023 database).

Scanning transmission electron microscopy (STEM) images were taken of the calcined catalysts, using a JEOL JEM-2200FS aberration corrected high resolution electron microscope operating at a 200 kV acceleration voltage. For the microscopy measurements, the samples were drop-casted with acetone on copper grids and coated with ultrathin carbon film. Elemental mappings were carried out with an X-ray energy-dispersive spectrometer (EDS), which was coupled to the microscope. For the Rh and Pt catalysts, the diameter of approximately 100 metal particles were measured using the ImageJ software to estimate the particle size distribution and the mean Pt and Rh particle size.

Pulse chemisorption measurements were carried out for 100 mg catalyst samples to estimate the mean metal particle size and dispersion. CO was used as a probe molecule for Ru/ZrO₂, Pt/ZrO₂ and Pd/ZrO₂,

whereas H₂ was used for Ni/ZrO₂ and Rh/ZrO₂. The measurements were done in an AMI-200R flow through equipment (Altamira Instruments), connected to an OmniStar GSD320 mass spectrometer (MS) (Pfeiffer Vacuum).

Prior to the pulse chemisorption, the samples of the calcined catalysts were dried at 200 °C in He for 120 min, reduced at 350 °C in 2 vol. % H₂/Ar for 60 min, cooled down to 50 °C and flushed for 60 min in He. Next, in case of CO pulse chemisorption, 25 pulses (0.505 ml) of 5 vol. % CO/He, were introduced to the samples with 5 min intervals, while monitoring the composition of the gas flow with the MS (*m/z* 28 for CO, 44 for CO₂ and 18 for H₂O). In the case of H₂ pulse chemisorption, 15 pulses (0.505 ml) of 4 vol. % H₂ were introduced to the samples with 10 min intervals, while monitoring *m/z* 2 for H₂. The temperature of the pulse loop was 100 °C during the CO pulse chemisorption measurements, and 30 °C during the H₂ pulse chemisorption measurements. The carrier gas flow was maintained at 50 ml/min (STP) throughout the measurement. The relations presented in the Handbook of Heterogeneous Catalysis were used to estimate the dispersion *D* (%) and mean particle size *d_m* (nm) from the adsorbed amount of probe gas.⁴¹ An adsorption stoichiometry of 1 was assumed for CO, whereas the adsorption stoichiometry for H₂ was assumed to be 2.

Hydrogen temperature-programmed reduction (H₂-TPR) was carried out for 120 mg samples of the calcined catalysts to study the reduction temperatures of the metals. The measurements were done in the AMI-200R equipment connected to the OmniStar GSD320 MS. The samples were heated from room temperature to 200 °C in He flow with a heating rate of 10 °C/min, and maintained there for 120 min, in order to remove moisture. Afterwards, the samples were cooled down to 30 °C in He flow. At 30 °C, the samples were flushed in Ar for 30 min. Next, a flow of 2 vol. % H₂/Ar was introduced to the reactor, and the temperature was elevated from 30 °C to 600 °C with a heating rate of 5 °C/min. The total flowrate was maintained at 50 ml/min (STP) throughout the measurement. The data between 30 and 50 °C was disregarded in the data treatment and visualization, due to signal fluctuations attributed to stabilization of the flowrates. To *m/z* 2 was followed with the MS in order to monitor the H₂ consumption. Additionally, *m/z* 4 (He), 18 (H₂O), 28 (N₂/CO), 32 (O₂) and 40 (Ar) were followed.

X-ray photoelectron spectroscopy (XPS) measurements were performed for the catalysts with a Kratos AXIS Ultra DLD X-ray photoelectron spectrometer using a monochromated Al_{Kα} X-ray source (1486.7 eV) run at 100 W. A pass energy of 80 eV and a step size of 1.0 eV were used for the survey spectra, while a

pass energy of 20 eV and a step size of 0.1 eV were used for the high-resolution spectra. Photoelectrons were collected at a 90° take-off angle under ultra-high vacuum conditions, with a base pressure typically below 1×10^{-9} Torr. The diameter of the beam spot from the X-ray was 1 mm, and the area of analysis for these measurements was 300 $\mu\text{m} \times 700 \mu\text{m}$. Both survey and high-resolution spectra were collected from three different spots on each sample surface in order to check for homogeneity and surface charge effects. The spectra were charge-corrected relative to the position of C–C bonding of carbon at 284.8 eV. Data analysis was carried out with the CasaXPS software. The catalyst samples were reduced ex situ at 350 °C in 2 vol. % H_2/Ar for 60 min before the measurements and transferred to the equipment exposed to air.

The Zr 3d spectra were fitted with two doublets, with the $3d_{5/2}$ peaks located at 181.8 eV and 183.0 eV. The lower binding energy component corresponds to a pure metal oxide, while the higher binding energy component was assigned to a mixed oxide state with a slightly lower electron density surrounding the Zr ions. The O 1s spectra were deconvoluted using three Gaussian components with equal full width at half maximum (FWHM). The most prevalent component corresponds to lattice oxygen of the support, followed by a component attributed to surface hydroxyls at a slightly higher binding energy (+1.5 eV). Furthermore, a minor component at higher binding energies (approximately 533.3 eV) was used, most likely attributed to oxygen bound to organic contaminants. The C 1s spectra were fitted with four Gaussian components according to standard tabulated chemical shifts, with peak positions at 284.8 eV (C–C), 286.5 eV (C–O), 287.8 eV (C=O), and 288.9 eV (O–C=O), corresponding to adventitious carbon. For the Ru/ZrO₂ catalyst, a deconvolution of the C 1s components was done together with the Ru 3d components, due to the overlap in the binding energy for these photoelectrons.

The Pt 4f spectrum of the Pt/ZrO₂ catalyst was fit using five doublets, for metallic Pt(0), Pt(I), Pt(II), Pt(IV), and for a mixed state located between Pt(I) and Pt(II). The binding energies for the Pt $4f_{7/2}$ of these components were located at 70.9 eV, 72.1 eV, 73.4 eV, 74.4 eV, and 72.4 eV, respectively. The Pd 3d spectrum of the Pd/ZrO₂ catalyst was fit with two doublets at $3d_{5/2}$ energies at 335.3 eV and 336.8 eV, corresponding to metallic Pd(0) and Pd(II). The Pd 3d spectrum overlaps with the Zr 3p spectrum, but the Pd $3d_{1/2}$ component was clearly visible between the peaks for the Zr 3p doublet, thereby allowing for the deconvolution of the smaller palladium components. The Ni 2p spectrum of the Ni/ZrO₂ catalyst was deconvoluted using three components corresponding to Ni(0), Ni(II) and Ni(III), with the $2p_{3/2}$ peaks at energies 852.8 eV, 853.9 eV, and 856.3 eV, respectively. Two doublets were used to deconvolute the Rh 3d spectrum of the Rh/ZrO₂ catalyst, at $3d_{5/2}$ energies of 307.2 eV and 308.8 eV, corresponding to Rh(0)

and Rh(III). The deconvolution of the Ru 3d spectrum of the Ru/ZrO₂ catalyst was complicated by the overlap with the C 1s spectrum. Two doublets with the 3d_{5/2} energies at 279.8 eV and 280.9 eV were used, corresponding to Ru(0) and Ru(IV), respectively. The binding energies of the transition metals components were in agreement with values given for similar components in the NIST database.⁴²

The overall basicity of the calcined catalysts and the ZrO₂ support was characterized through temperature-programmed desorption of CO₂ (CO₂-TPD). The measurements were done with the AMI-200R equipment connected to the OmniStar GSD320 MS, for 150 mg catalyst samples. A 50 ml/min (STP) flow was maintained throughout the experiment. The samples were dried in He for 2 hours at 180 °C, using a heating ramp of 10 °C/min. The samples were then cooled down to 50 °C in He and further held for 30 min. Next, a 1 vol. % CO₂/He flow was directed through the samples at 50 °C for 30 min, which was followed by a He flush for 60 min. Then, the samples were heated to 800 °C in He with a heating rate of 10 °C/min, and kept at 800 °C for 30 min before cooling down. The MS was used for data acquisition, following *m/z* 44 for CO₂. Additionally, *m/z* 28 (CO), 18 (H₂O), 32 (O₂) and 4 (He) were followed.

Acid site characterization was carried out for the calcined catalysts with Fourier transform infrared spectroscopy (FTIR), using pyridine as the probe molecule. A Thermo Scientific Nicolet iS10 spectrometer, equipped with an in situ transmission FTIR cell by Harrick Scientific Products Inc (customized from the HTC-3 model), a liquid-N₂ cooled Mercury-Cadmium-Telluride (MCT) detector and HeNe laser was used for the measurements. The spectra range was 4000-650 cm⁻¹ and a spectral resolution of 0.24 cm⁻¹ was used.

The catalyst samples (25 mg) were pressed into self-supported pellets, 1.1 cm in diameter, with a hydraulic press. The samples were heated in vacuum to 90 °C with a 5 °C/min heating ramp, and maintained there for 30 min. Next, the temperature was elevated to 450 °C with a 20 °C/min ramp and kept there for 60 min. The temperature was then lowered to 170 °C and held for 10 min, after of which the spectra of the clean samples were recorded. Next, the samples were saturated with pyridine for 10 min, using an atmospheric saturator, which was followed by evacuation and a 15 min hold. After that, the spectra that were used to quantify the acidity were recorded.

The Omnic 9.11 software was used to subtract the background and the spectra of the clean sample from the pyridine-saturated sample. Peak integration and deconvolution were carried out with Omnic 9.11 and

OriginPro. The concentration of Lewis and Brønsted acid sites was estimated from the peak areas and sample weight, using the relations presented by Emeis.⁴³

2.4 Catalytic Activity Tests. The catalytic activity tests were carried out in a 100 ml Hastelloy high-pressure batch reactor by Parr Instrument Company, which was equipped with a heated feed vessel. The experimental conditions were similar as in previous works by Verkama et al.^{27,28}

A 20 mg catalyst sample was first dried in situ at 180 °C under 10 bar of N₂ for 60 min, and then reduced at 350 °C under 20 bar of H₂ for 60 min. The feed mixtures were prepared by dissolving 56.5 mg of *n*-hexadecanamide or 53.5 mg of 1-hexadecylamine to 31 ml of decalin under heating, targeting an initial nitrogen concentration of 100 ppm. A 1 ml zero-sample was taken for analysis, and the feed mixture was transferred to the heated feed vessel attached to the reactor. The reactor was heated to 300 °C, and the feed mixture was released to the reactor from the feed vessel. The reactor was then pressurized to 80 bar H₂, and stirring at 600 rpm was initiated, which marked the onset of the reaction time. The reaction was quenched with ice and the stirring was stopped, once the reaction time (15-300 min) had elapsed. A reference reaction time of 60 min was used for the comparison of the catalysts and model compounds. The reactions with different reaction times were visualized as a function of batch residence time τ ($\text{g}_{\text{cat}}\text{h}/\text{g}_{\text{amide}}$), as defined in Equation (1), to account for variations in the initial amounts of catalyst and reactant.

$$\tau = \frac{m_{\text{cat}}t}{m_{\text{A}}} \quad (1)$$

Here, m_{cat} is the mass of catalyst (g), t is the reaction time (h) and m_{A} is the mass of reactant at the start of the reaction (g).

Thermal tests and experiments with the bare ZrO₂ support were done for both model compounds. A set of control experiments, described and reported in a previous work by Verkama et al.,²⁷ were carried out for the Pt/ZrO₂ catalyst.

2.5 Analysis of the Liquid Reaction Products. A second solvent (2-propanol) and an internal standard (*n*-dodecane) were added to the samples prior to analysis. The second solvent was needed to prevent precipitation of the reactant and the products.

A Shimadzu QP2010SE gas chromatograph-mass spectrometer (GC-MS) with EI ionization and an Optic 4 injector was used to identify the products. The GC-MS was equipped with an Agilent J&W HP5-MS column (30 m × 0.25 mm × 0.25 μm), and the NIST2017 library was used to match the fragmentation patterns.

Quantification of the liquid products was carried out with an Agilent 7890 gas chromatograph (GC), equipped with an Agilent J&W HP5-MS column (30 m × 0.25 mm × 0.25 μm), with the outlet split to a flame ionization detector (FID) and a nitrogen phosphorus detector (NPD). The inlet of the GC was at 325 °C, as was the temperature of both the FID and the NPD. An injection volume of 2 μl and a split ratio of 5:1 was used. The analysis program started with a 3 min hold at 40 °C, from where the temperature first was elevated to 100 °C with a ramp of 20 °C/min and held there for 3 min. The temperature was next elevated to 150 °C with a ramp of 5 °C/min, and from there to 325°C with a ramp of 10 °C/min, where a final 12 min hold took place.

Weight-based FID response factors, relative to the internal standard *n*-dodecane, were determined experimentally for *n*-pentadecane, *n*-hexadecane, 1-hexadecylamine, 1-hexadecanol, palmitic acid, *n*-hexadecanamide, *n*-pentadecanonitrile and *n*-heptadecanonitrile. The response factors for *n*-pentadecanonitrile and *n*-heptadecanonitrile were averaged to obtain an estimate for the response factor of *n*-hexadecanonitrile. The response factors for *n*-hexadecanal, *n*-hexadecyl hexadecylamine, *n*-hexadecyl hexadecanamide, dipentadecyl ketone, palmityl palmitate and propyl hexadecylamine were estimated using their combustion enthalpy, according to the procedure presented by de Saint Laumer et al.⁴⁴

The reactant conversion X_A (%) was calculated with Equation (2),

$$X_A = \frac{n_{A,0} - n_A}{n_{A,0}} \cdot 100\%, \quad (2)$$

where $n_{A,0}$ is the initial amount of reactant (mol) and n_A is the amount of unreacted reactant in the product sample (mol).

The yield for each product Y_P (%) was calculated with Equation (3),

$$Y_P = \frac{\mu_P n_P}{n_{A,0}} \cdot 100\%, \quad (3)$$

where μ_P is a stoichiometric factor (2 for the C32 compounds and 1 for the other products) and n_P is the amount of product P in the product sample (mol).

The oxygen removal (*O-removal*, %) of the C16 amide experiments was estimated from the product distribution, according to Equation (4),

$$O\text{-removal} = \frac{c_{O,\text{products}}}{c_{O,\text{feed}}} \cdot 100\%, \quad (4)$$

where $c_{O,\text{products}}$ (ppm) and $c_{O,\text{feed}}$ (ppm) are the oxygen contents of the product sample and feed mixture, respectively, based on the amounts of oxygen-containing compounds that were detected from the GC-FID analysis.

The molar carbon balance closure B_C was calculated using Equation (5),

$$B_C = \frac{n_{C,\text{products}}}{n_{C,\text{feed}}} \cdot 100\%, \quad (5)$$

where $n_{C,\text{products}}$ is the amount of carbon quantified from the product mixture (mol) and $n_{C,\text{feed}}$ is the amount of carbon quantified from the feed mixture (mol). The molar carbon balance closure was generally above 90%.

The total nitrogen content of the liquid samples was analyzed with an AntekPAC EleMeNtS analyzer, calibrated for nitrogen contents between 0 and 1000 ppm with standard calibration solutions (AC Analytical Controls BV). The nitrogen removal (*N-removal*, %) was calculated using Equation (6),

$$N\text{-removal} = \frac{c_{N,\text{products}}}{c_{N,\text{feed}}} \cdot 100\%, \quad (6)$$

where $c_{N, \text{products}}$ is the nitrogen content of the product sample (ppm) and $c_{N, \text{feed}}$ is the nitrogen content of the feed mixture (ppm).

2.6 Gas Phase Analysis. A gas phase sample was collected to a bomb after the reactor had cooled down. The gas phase was qualitatively analyzed with an Agilent 6890 permanent gas GC. Non-condensable gases were separated with HP-PLOT and HP-Molesieve columns, using Ar as the carrier gas, and were detected with a TCD. The hydrocarbons were separated with a HP-AL/KCL column using He as the carrier gas and detected with an FID. Each sample was analyzed three times.

3. Results and Discussion

3.1 Catalyst Characterization. Table 1 displays the BET specific surface area, pore volume and mean pore diameter obtained from N₂-physisorption measurements of the calcined catalysts, and the CO or H₂ adsorption capacity, mean metal particle size and dispersion obtained from pulse chemisorption measurements of the reduced catalysts.

Table 1. Properties of the catalysts based on N₂-physisorption measurements and pulse chemisorption measurements

Catalyst	N ₂ -physisorption ^a			Pulse chemisorption ^b		
	S _{BET} (m ² /g)	V _{pore} (cm ³ /g)	d _{pore} (nm)	CO/H ₂ ads. capacity (μmol/g _{cat})	d _m (nm)	D (%)
ZrO ₂	47	0.25	20	-	n.a.	n.a.
Ni/ZrO ₂	48	0.23	20	3 ^d	30 ^d	4% ^d
Pd/ZrO ₂	50	0.27	19	36 ^c	2.9 ^c	38% ^c
Pt/ZrO ₂	42	0.25	19	30 ^c	1.9 ^c	59% ^c
Rh/ZrO ₂	45	0.23	20	25 ^d	2.2 ^d	50% ^d
Ru/ZrO ₂	48	0.26	20	61 ^c	2.1 ^c	61% ^c

^aThe measurements carried out for the calcined catalysts

^bThe catalysts were reduced at 350 °C in H₂ before the measurements

^cBased on CO pulse chemisorption

^dBased on H₂ pulse chemisorption

n.a. = not applicable

The semi-quantitative XRF measurements indicated a metal loading of 0.6 wt. % for Pd/ZrO₂ and Pt/ZrO₂, and a metal loading of 0.7 wt. % for Ni/ZrO₂, Rh/ZrO₂ and Ru/ZrO₂. These values were within the measurement uncertainty of each other. The catalysts displayed IUPAC Type IV(a) N₂-physisorption isotherms, with a Type H2(b) hysteresis loop.⁴⁵ The BET specific surface area (42-50 m²/g), pore volume (0.23-0.27 cm³/g) and mean pore diameter (19-20 nm) of the catalysts and the bare support were similar, indicating that impregnation of the active metal did not alter the morphology significantly (Table 1). The N₂-physisorption isotherms and BJH pore size distribution of the catalysts and the support are displayed in Figure S1 and Figure S2 of the Supporting Information. The X-ray diffractograms of the calcined catalysts only contained reflections related to monoclinic ZrO₂ (ICDD 00-007-0343), suggesting that the active metals were well dispersed before reduction.⁴⁶ The X-ray diffractograms of the calcined catalysts and the ZrO₂ support are available in Figure S3 of the Supporting Information.

The reduction temperatures of the active metals were studied via H₂-TPR measurements of the calcined catalysts. The H₂-TPR profiles of the catalysts and the ZrO₂ support are presented in Figure 1.

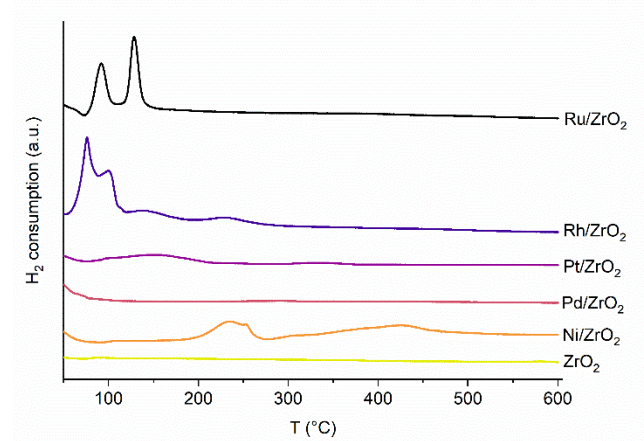


Figure 1. H₂-TPR profiles of the calcined catalysts and the ZrO₂ support. The data has been vertically shifted for clarity.

No reducible species were detected on the bare ZrO₂ support (Figure 1). The H₂-TPR profile of Ni/ZrO₂ had three major reduction peaks. The first and second peaks reached their maximum intensity at 237 °C and 257 °C, respectively. The third broad and shallow reduction peak reached its maximum intensity at 425 °C, i.e., above the reduction temperature that was used for the activity tests (350 °C). The first reduction peaks were likely related to the reduction of NiO particles with relatively weak interactions with the ZrO₂ support.^{37,47–49} The higher temperature peak may have involved the reduction of NiO particles interacting more strongly with the ZrO₂ support, or the reduction of Ni²⁺ species in the ZrO₂ lattice.^{37,47–49} It is possible that a part of the Ni remained oxidic at the end of the H₂-TPR measurement.⁵⁰

The H₂-TPR profile of Pd/ZrO₂ did not contain any major reduction peaks, but the H₂ consumption signal was elevated from the start of the ramp until approximately 100 °C (Figure 1). This could suggest that the PdO got reduced immediately upon the introduction of H₂, or that the Pd was in its reduced state already after calcination.⁵¹ The H₂-TPR profile of Pt/ZrO₂ contained a broad and shallow reduction peak around 140 °C, which probably involved the reduction of PtO₂ to metallic Pt.^{52,53}

Multiple reduction peaks were present in the H₂-TPR profile of Rh/ZrO₂ (Figure 1). The reduction of Rh₂O₃ particles to metallic Rh mainly occurred below 130 °C, as observed from the major reduction peaks at 75 and 98 °C.^{54–58} The two smaller reduction peaks at 140 and 230 °C may have been attributed to reduction

of larger Rh₂O₃ particles, Rh₂O₃ particles interacting more strongly with the support, or to Rh-assisted partial reduction of the ZrO₂ support.^{54–58}

The H₂-TPR profile of Ru/ZrO₂ contained reduction peaks at 90 and 130 °C, and no H₂ consumption was observed at temperatures above 150 °C (Figure 1). Similar H₂-TPR profiles have been reported for Ru/ZrO₂ catalysts in the literature.^{59–61} The first peak has been explained by the reduction of RuO₂ particles to metallic Ru, whereas the second peak has been proposed to involve the reduction of RuO₂ particles with stronger interactions with ZrO₂.^{59–61} The H₂-TPR measurements therefore indicated that the Ru, Rh, Pt and Pd got reduced during the reduction treatment that was used before the activity tests, whereas part of the Ni possibly remained oxidic.

Based on the pulse chemisorption measurements, the mean metal particle size ranged between 1.9 and 2.9 nm for Pt/ZrO₂, Pd/ZrO₂, Ru/ZrO₂ and Rh/ZrO₂, whereas the dispersions varied from 38 to 61% (Table 1). Due to the uncertainty of the semi-quantitative elemental analysis, the dispersion and mean particle size were calculated based on the nominal metal loading (1 wt. %), which implies that the dispersion and mean particle size of the Pt, Pd, Ru and Rh catalysts are within the measurement accuracy of each other. Based on the H₂ pulse chemisorption measurement, the mean particle size (30 nm) and dispersion (4%) of Ni/ZrO₂ deviated from the noble metals significantly. Considering the relatively high reduction temperature (Figure 1) and the absence of Ni-related reflections in the X-ray diffractogram of the calcined Ni/ZrO₂ catalyst, it is possible that the low H₂ adsorption capacity partly was related to an incomplete reduction of Ni. A selection of representative STEM images with elemental EDS mappings is available in Figure S4 of the Supporting Information. The mean metal particle size derived from the STEM images was 2.1 nm for both Pt/ZrO₂ and Rh/ZrO₂, which is in good agreement with the pulse chemisorption results (Table S1, Supporting Information). Due to an insufficient contrast between the active metal and the support, the active metal particle size distribution could not be reliably estimated from the STEM images of the Ru, Pd and Ni catalysts.

XPS measurements were carried out for the catalysts and the bare ZrO₂ support to study the chemical state of the active metals and their interactions with the support. The catalyst samples were reduced ex situ in H₂ at 350 °C before the measurements and transferred to the equipment exposed to air. The XPS survey spectra of the samples are available in Figure S5 of the Supporting Information. Figure 2 presents high-resolution XP spectra of the Ni 2p (a), Pd 3d (b), Pt 4f (c), Rh 3d (d) and Ru 3d (e) regions of the

Ni/ZrO₂, Pd/ZrO₂, Pt/ZrO₂, Rh/ZrO₂ and Ru/ZrO₂ catalysts, respectively. Table 2 summarizes the surface composition of the catalysts, and the relative amounts of active metal in reduced and oxide states.

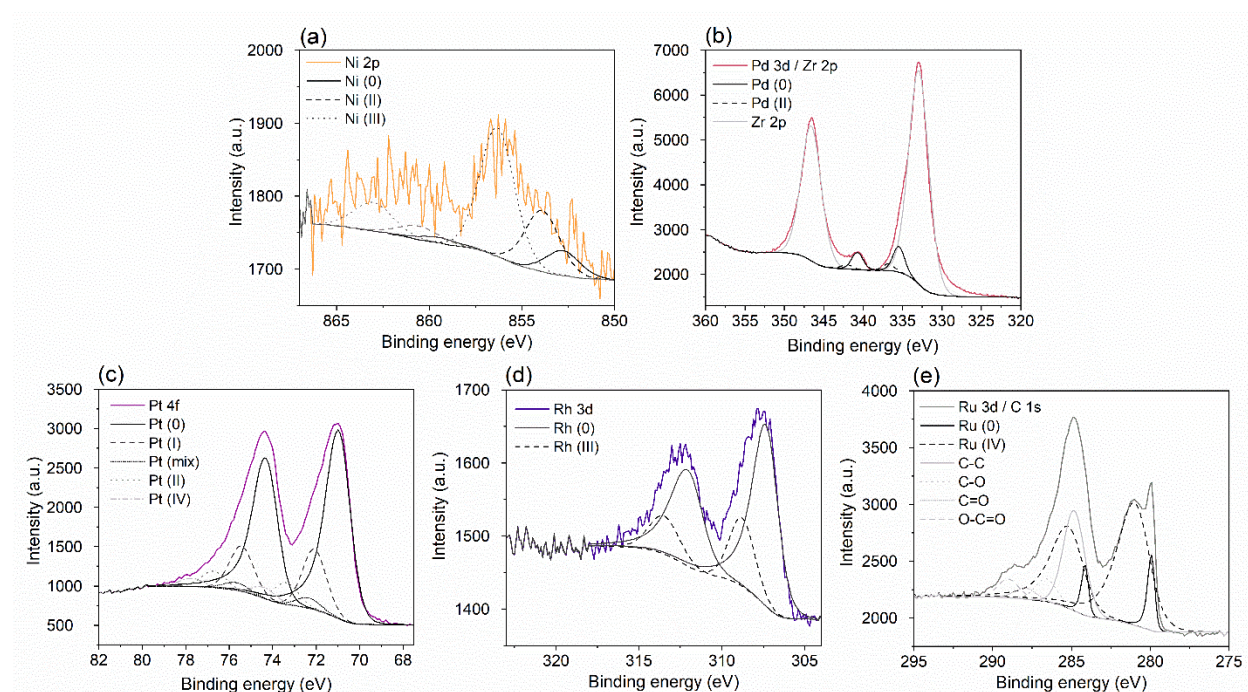


Figure 2. High-resolution X-ray photoelectron spectra of (a) the Ni 2p region of Ni/ZrO₂, (b) the Pd 3d / Zr 2p region of Pd/ZrO₂, (c) the Pt 4f region of Pt/ZrO₂, (d) the Rh 3d region of Rh/ZrO₂ and (e) Ru 3d / C 1s region of Ru/ZrO₂. The samples were reduced ex situ in H₂ at 350 °C before the XPS measurements and transferred to the equipment exposed to air.

Table 2. XPS-derived atomic surface composition and relative amounts of active metal M in reduced state M(0) and in oxidic states M(ox.)

Catalyst ^a	Atomic surface composition ^b				Oxidation states	
	M (at. %)	Zr (at. %)	O (at. %)	C (at. %)	M(0) (%)	M(ox.) (%)
ZrO ₂	-	30.1	46.4	22.3	-	-
Ni/ZrO ₂	0.7	33.0	52.7	12.3	13.5%	86.5%
Pd/ZrO ₂	1.1	29.6	51.6	16.8	74.0%	26.0%
Pt/ZrO ₂	4.9	30.4	52.3	12.5	71.9%	28.1%
Rh/ZrO ₂	0.8	33.1	53.9	8.0	74.5%	25.5%
Ru/ZrO ₂	3.0	28.8	51.8	15.5	14.1%	86.0%

^aThe samples were reduced ex situ in H₂ at 350 °C before the XPS measurements and transferred to the equipment in atmosphere.

^bThe XPS measurement indicated that the Rh/ZrO₂ catalyst also contained 2.8 at. % potassium.

The catalysts showed differences in the surface concentration of active metal and in their oxidation states (Table 2). Pt/ZrO₂ and Ru/ZrO₂ had the highest metal surface concentration, with 4.9 at. % Pt and 3.0 at. % Ru. The surface concentration of active metal was lower for Pd/ZrO₂, Rh/ZrO₂ and Ni/ZrO₂, 1.1, 0.8 and

0.7 at. %, respectively. Over 70% of the Pt, Pd and Rh was reduced, while more than 85% of the Ru and Ni was oxidic (Table 2, Figure 2). Considering the H₂-TPR profiles (Figure 1), where the Pt, Pd, Rh and Ru-related reduction peaks were located below 350 °C, i.e., the temperature that was used for the ex situ sample reduction, the partial surface oxidation of the noble metals may be related to the exposure to air during the sample transfer to the XPS. The high degree of oxidation of Ru therefore suggests that the metal got oxidized easier than the other noble metals, reflecting the intrinsic redox potential of Ru. Similar results have been reported for supported Ru catalysts elsewhere.⁶² Based on H₂-TPR, the relatively high degree of oxidation of Ni/ZrO₂, i.e. the only base metal catalyst, was expected.

The catalysts exhibited some differences in the state of the ZrO₂ support and in the Zr 3d and O 1s binding energies, potentially reflecting electron transfer between the active metals and the support. Notably, the Zr 3d and O 1s binding energies on Rh/ZrO₂ were approximately 0.3 eV lower compared to the bare ZrO₂ support, which may indicate electron transfer from Rh to the support. Table S2 of the Supporting Information displays the oxidation states of ZrO₂, while Figures S6a and S6b of the Supporting Information present the high resolution XPS spectra of the Zr 3d and O 1s regions, respectively.

Basic and acid site characterization were carried out via CO₂-TPD measurements and FTIR spectroscopy of pyridine adsorption, respectively. Figure 3a displays the CO₂-TPD profiles, while the transmission FTIR spectra of the pyridine-saturated catalysts (170 °C) with the spectra of the clean samples and the background subtracted are presented in Figure 3b.

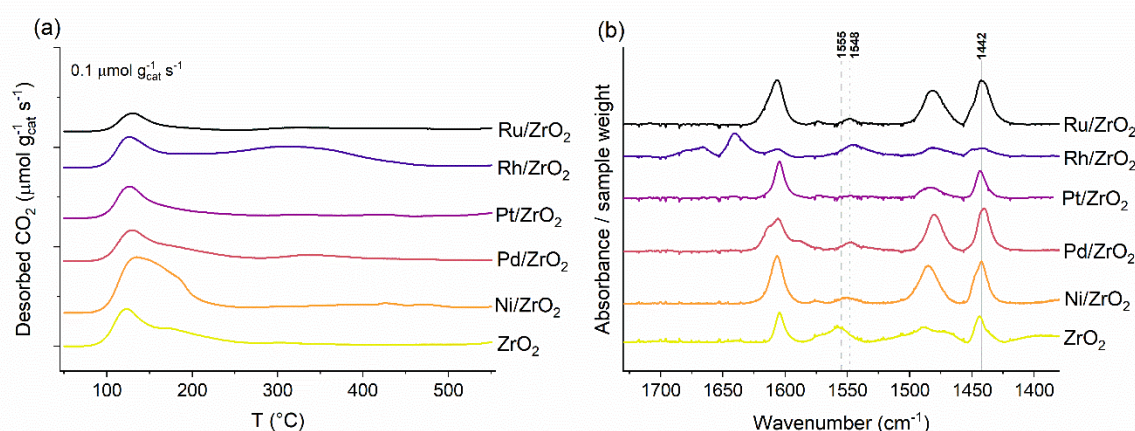


Figure 3. Analysis of the calcined catalysts via (a) CO₂-TPD and (b) transmission FTIR of adsorbed pyridine. The spectra of the clean samples and the background have been subtracted from the spectra of the pyridine-saturated samples. The vertical lines indicate the vibration bands characteristic for pyridine adsorbed on Lewis acid sites (1442 cm⁻¹) and Brønsted acid sites (1548 and 1555 cm⁻¹). The data has been vertically shifted for clarity.

Based on the CO₂ desorption profiles (Figure 3a), the CO₂ adsorption strength and CO₂ adsorption capacity were similar for the bare ZrO₂ support (36 μmol/g), Pd/ZrO₂ (36 μmol/g) and Pt/ZrO₂ (30 μmol/g). This suggests that the adsorption of CO₂ on Pt/ZrO₂ and Pd/ZrO₂ mainly occurred on the support. The CO₂ desorption profiles contained a broad peak with maximum intensity at 120 °C and a shoulder at approximately 150 °C. The CO₂ may have adsorbed as bicarbonate species on Brønsted basic OH groups, as monodentate carbonate species on Lewis basic O²⁻ centers and as bidentate carbonate species on Lewis acid–base (Zr⁴⁺-O²⁻) pairs.^{47,63} The bidentate carbonate species likely accounted for the shoulder at 150 °C.⁶³ The CO₂ adsorption capacity of the Ru/ZrO₂ catalyst (16 μmol/g) was less than half compared to the bare ZrO₂ support, and the desorption peak did not contain the shoulder at 150 °C, indicating that the impregnation of Ru suppressed the amount of the strongest basic sites or acid–basic site pairs of the ZrO₂ support.

The CO₂ adsorption capacity of Ni/ZrO₂ (63 μmol/g) and Rh/ZrO₂ (66 μmol/g) was approximately 30 μmol/g higher compared to the bare ZrO₂ support, which suggests that the CO₂ partly adsorbed on the active metals or the interface between the active metal and the support (Table 1). The CO₂ desorption peak of Ni/ZrO₂ was in a similar temperature range as for the ZrO₂ support, but a relatively larger share of the CO₂ desorption occurred above 150 °C (Figure 3a). The CO₂ desorption profile of Rh/ZrO₂ contained both the peak around 120 °C, related to CO₂ adsorbed on ZrO₂, and a broad peak which reached maximum intensity around 300 °C. The high-temperature peak may be related to CO₂ that was adsorbed on Rh, but might also be related to the K on the catalyst surface (Table 2).⁶⁴ Based on the desorption temperature, the basic sites on the Rh/ZrO₂ catalyst were considerably stronger compared to the other catalysts.

As described previously, Lewis and Brønsted acid sites are mechanistically involved in several reactions of the amide hydrotreatment reaction network.²⁷ The total acid site concentration was 80 μmol/g or lower for the studied catalysts, and the vibration bands characteristic for pyridine adsorbed on Lewis acid sites and Brønsted acid sites were located at 1442 cm⁻¹ and 1548 cm⁻¹, respectively (Figure 3b). Therefore, the ZrO₂-supported catalysts had a relatively low acid site concentration, and the acid sites were weak compared to catalysts supported on other inorganic oxides, such as γ-Al₂O₃, SiO₂-Al₂O₃ and TiO₂.^{65,66} The bare ZrO₂ support had 40 μmol/g Brønsted acid sites and 30 μmol/g Lewis acid sites. The impregnation of Pt, Pd, Ni and Ru suppressed the Brønsted acid site concentration to less than 20 μmol/g, whereas the Lewis acid site concentration was unaffected for Pt/ZrO₂ and increased to 60-70 μmol/g for Pd/ZrO₂,

Ni/ZrO₂, and Ru/ZrO₂. The differences in the acidity of these catalysts fell within the measurement uncertainty and are not expected to have a significant influence on the catalytic activity.

Rh/ZrO₂ was the only catalyst where the concentration of Brønsted acid sites (40 μmol/g) exceeded the concentration of Lewis acid sites (20 μmol/g). It is possible that the K on the catalyst surface (Table 2) suppressed the Lewis acidity of the catalyst.⁶⁷ The acid–base properties of Rh/ZrO₂ therefore deviated from the other catalysts.

3.2 Catalytic Hydrotreatment of *n*-Hexadecanamide. Hydrotreatment experiments were carried out at 300 °C and 80 bar H₂, using *n*-hexadecanamide (C16 amide) as the model compound and a reaction time of 60 min. The main products of the C16 amide hydrotreatment experiments were *n*-pentadecane (C15 paraffin), *n*-hexadecane (C16 paraffin), *n*-hexadecanal (C16 aldehyde), 1-hexadecylamine (C16 amine), 1-hexadecanol (C16 alcohol), *n*-hexadecanonitrile (C16 nitrile), palmitic acid (C16 acid), dipentadecyl ketone (31 ketone), *n*-hexadecyl hexadecylamine (C32 amine), palmityl palmitate (C32 ester) and *n*-hexadecyl hexadecanamide (C32 amide). Figure 4 displays the product distribution, conversion, nitrogen removal and oxygen removal of the C16 amide hydrotreatment experiments. The nitrogen removal was obtained from the total nitrogen content analysis, while the oxygen removal was derived from the GC data.

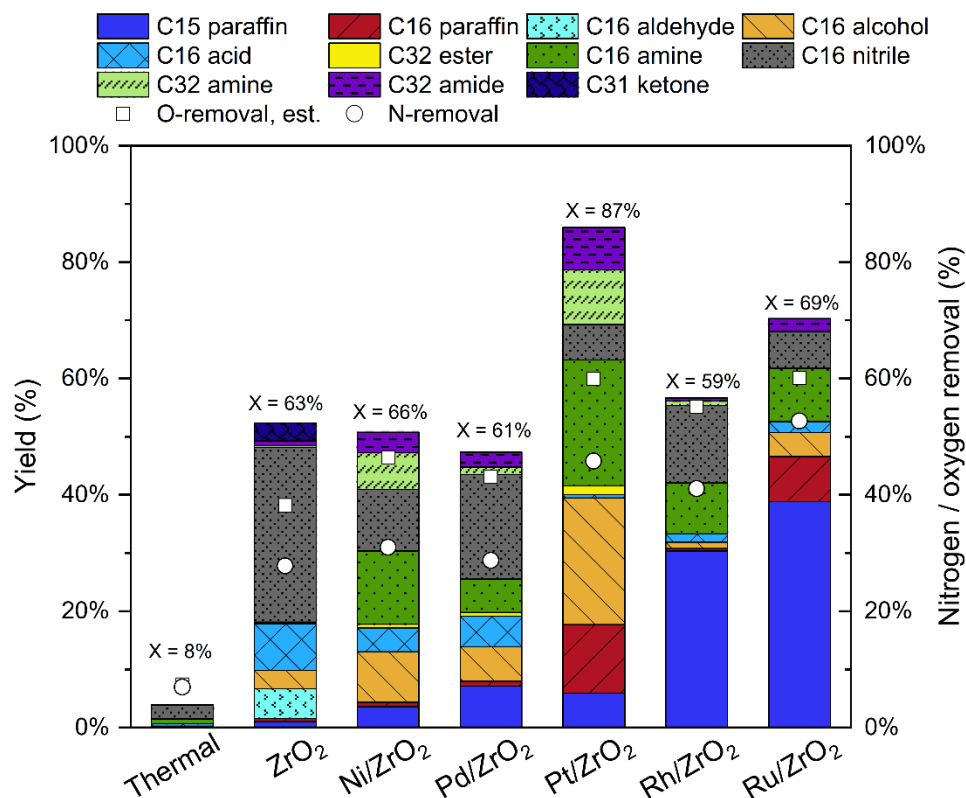
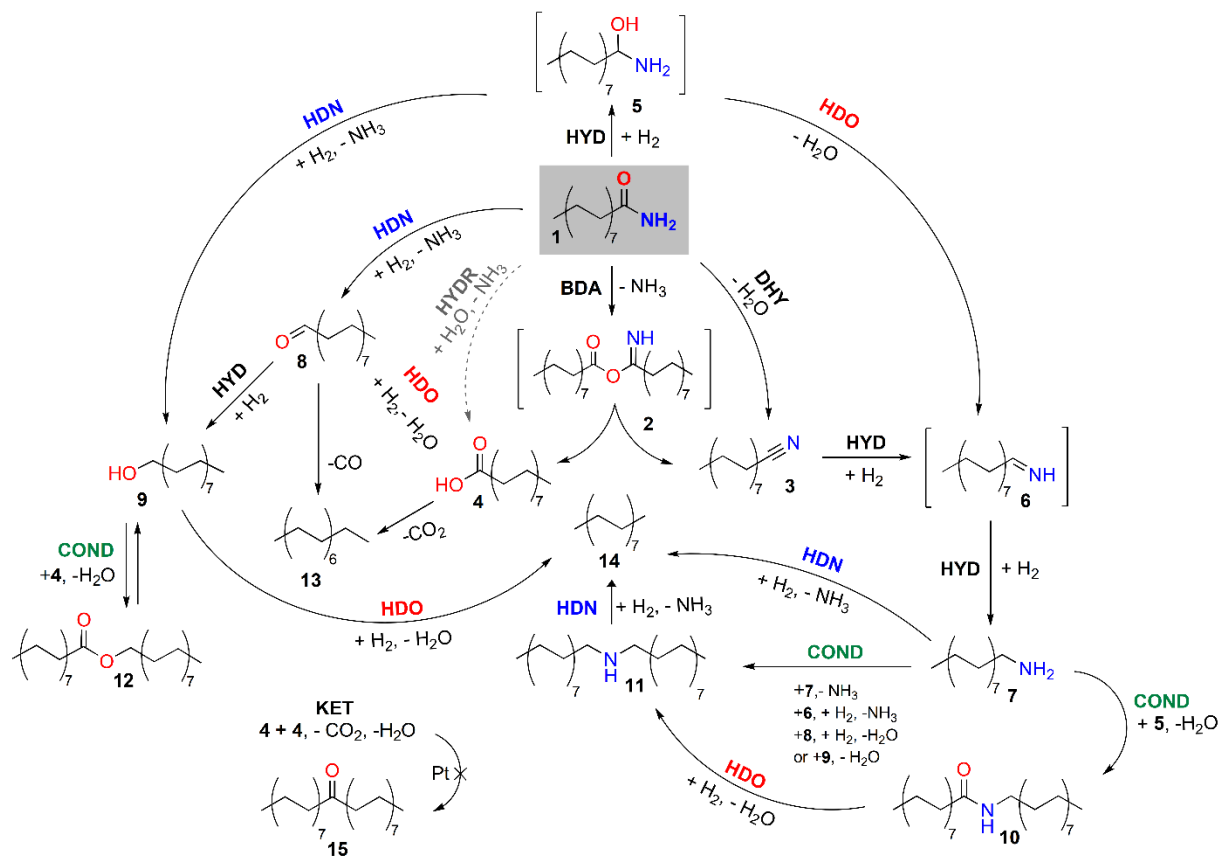


Figure 4. Product distribution, conversion, nitrogen removal (○) and oxygen removal (□) in the hydro-treatment of the C16 amide. The experiments were carried out at 300 °C and 80 bar H₂ for 60 min, stirring 600 rpm and using an initial nitrogen content of 100 ppm. The nitrogen removal was obtained from the total nitrogen content analysis, while the oxygen removal was derived from the product distribution.

The studied catalysts and the bare ZrO₂ support exhibited activity for the conversion of the C16 amide (Figure 4). The nitrogen removal of the 60 min reference experiments increased in the order of ZrO₂ (28%), Pd (29%), Ni (31%) << Rh (41%) < Pt (46%) < Ru (53%). Based on the product distribution, the oxygen removal increased in the order of ZrO₂ < Pd < Ni << Rh < Pt ≈ Ru, reaching approximately 60% on the most active catalysts. The oxygen removal exceeded the nitrogen removal on the studied catalysts. Scheme 1 displays a proposed reaction network for the hydro-treatment of the C16 amide. The reaction network has been adapted and extended from previous works by Verkama et al.,^{27,28} by the addition of the reaction pathway for the conversion of the C16 amine to the C15 paraffin.



Scheme 1. Proposed reaction network for the hydrotreatment of *n*-hexadecanamide, including the reaction network for the hydrotreatment of 1-hexadecylamine. Indicated compounds: **1** C16 amide, **2** C32 isoimide **3** C16 nitrile, **4** C16 acid, **5** C16 hemiaminal, **6** C16 imine, **7** C16 amine, **8** C16 aldehyde, **9** C16 alcohol, **10** C32 amide, **11** C32 amine, **12** C32 ester, **13** C15 paraffin, **14** C16 paraffin, **15** C31 ketone. The bimolecular deammoniation (BDA), direct dehydration (DHY), hydrogenation (HYD) and hydrolysis (HYDR) of the C16 amide, and the condensation (COND), hydrodeoxygenation (HDO) and hydrodenitrogenation (HDN) reactions of the intermediates have been indicated. The disproportionation of the C16 amine is included in the condensation reactions. The bimolecular ketonization of the C16 acid (KET) only occurred on the bare support. Note that the C15 paraffin (**13**) is indicated in two locations. The reaction network has been adapted and extended from previous works by Verkama et al.^{27,28}

Hydrotreatment experiments with different batch residence times were conducted for the two most active catalysts, Pt/ZrO₂ and Ru/ZrO₂. Figure 5 displays the product distribution of Pt/ZrO₂ (a) and Ru/ZrO₂ (b) in the hydrotreatment of the C16 amide, as a function of batch residence time. The experiments were carried out at 300 °C and 80 bar H₂, using 20 mg catalyst and an initial nitrogen content of 100 ppm. The 60 min reference experiments of Figure 4 correspond to the batch residence time 0.37 g_{cat}h/g_{amide}. The product distribution of the different catalysts is discussed in the following paragraphs.

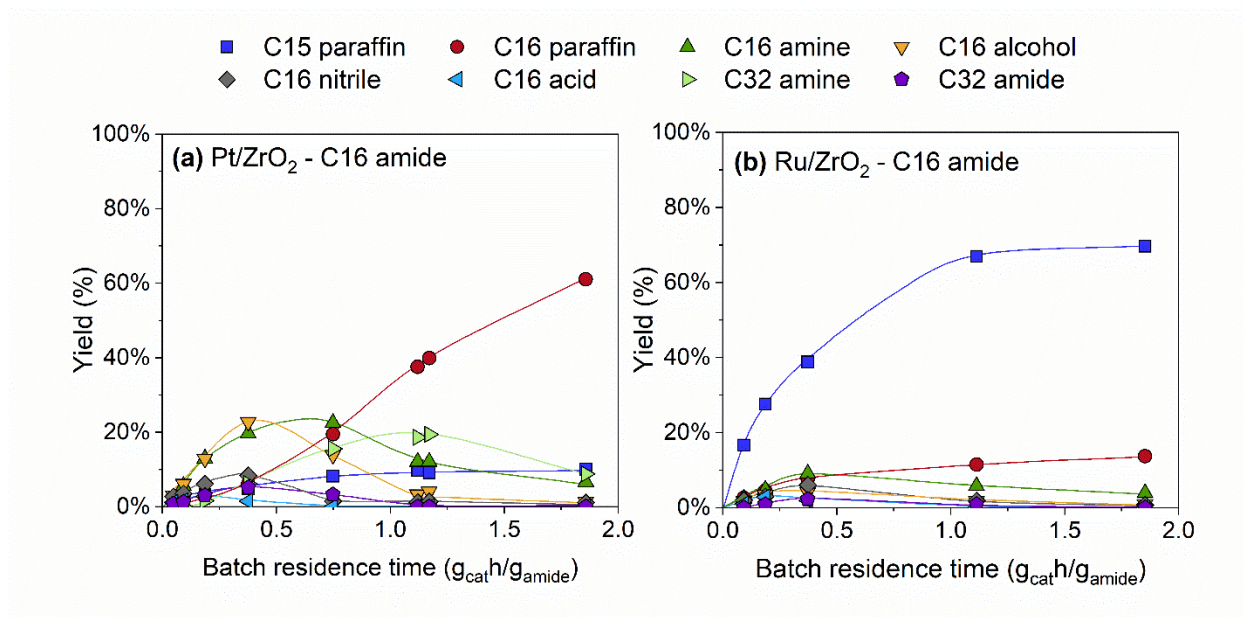


Figure 5. Product distribution as a function of batch residence time for (a) Pt/ZrO₂ and (b) Ru/ZrO₂ in the hydrotreatment of the C16 amide. The experiments were carried out at 300 °C, 80 bar H₂, using 20 mg of catalyst and an initial nitrogen content of 100 ppm. The trendlines have been added to guide the eye.

The bare ZrO₂ support exhibited activity for the conversion of the C16 amide to the C16 nitrile and C16 acid (Figure 4) via bimolecular deammoniation (BDA, Scheme 1). The reaction pathway has been described by Davidson and Karten.⁶⁸ The C16 amide may additionally have been converted to the C16 nitrile via dehydration and to the C16 acid via hydrolysis.⁶⁹ In line with literature, the BDA and dehydration of the C16 amide also occurred thermally, but with an approximately 90% lower activity compared to the ZrO₂ support.⁶⁸ Furthermore, the bare ZrO₂ support was active for the conversion of the C16 acid to the C16 aldehyde and the bimolecular ketonization of the C16 acid to the C31 ketone.^{70–72} A part of the C16 aldehyde was further converted to the C16 alcohol. The C31 ketone and the reactive C16 aldehyde were not present in the product samples of the metal catalysts.⁷¹ The activity of the ZrO₂ support and the active sites for the aforementioned reactions have been elaborated further previously.²⁷

In line with a previous work by Verkama et al.,²⁷ the product distribution and conversion of the C16 amide on the different catalysts (Figure 4) indicated that the initial C16 amide conversion route was significantly influenced by the ZrO₂ support (Scheme 1). This was particularly evident in the case of Pd/ZrO₂ and Ni/ZrO₂, which exhibited a similar activity and selectivity as the bare ZrO₂ support in the hydrotreatment

of the C16 amide. Meanwhile, the active metal was decisive for the activity and pathway selectivity for the conversion of the intermediate products via the hydrogenation and hydrogenolysis routes.

The main difference between the bare support and Pd/ZrO₂ was that Pd/ZrO₂ showed activity towards decarbonylation of the C16 aldehyde and/or decarboxylation of the C16 acid, resulting in a 7% C15 paraffin yield, and produced C16 alcohol and C16 amine through hydrogenation of the C16 aldehyde and C16 nitrile, respectively (Figure 4). The C16 amine and C16 alcohol yields were both 6% on Pd/ZrO₂, whereas only 1% of the C16 paraffin was formed. The amounts of CO and CO₂ were below the detection limit of the gas phase analysis, due to the low initial concentration of the model compound.

Ni/ZrO₂ showed a higher hydrogenation activity than Pd/ZrO₂, as indicated by the C16 amine and C16 alcohol yields of 13% and 9%, respectively (Figure 4). Similarly to Pd/ZrO₂, Ni/ZrO₂ only gave 1% of the C16 paraffin, but produced less C15 paraffin (4%). Ni/ZrO₂ produced more C32 amine compared to Pd/ZrO₂ (6% vs 1%), whereas the C32 amide yields were similar (3-4%). The molar carbon balance closure of the C16 amide experiments on Pd/ZrO₂ and Ni/ZrO₂ (~85%) was lower than for the other catalysts (>90%), potentially hinting towards the formation of heavy, nonvolatile products that could not be detected by GC-FID. For example, the formation of trihexadecylamine (C48 amine) may have occurred.⁷³⁻⁷⁶ The low activity of the Ni catalyst may have been related to the relatively low number of surface Ni sites (Table 1). Considering the low price of Ni compared to noble metals, it could be viable to increase the Ni loading in order to improve the catalytic activity.^{23,77,78}

The activity of Pt/ZrO₂ markedly exceeded the activity of Ni/ZrO₂ and Pd/ZrO₂, but the product distribution shared some similarities. Pt/ZrO₂ provided the highest conversion (87%) out of the studied catalysts in the hydrotreatment of the C16 amide (Figure 4). The hydrogenation activity of Pt/ZrO₂ was superior to the other catalysts, as suggested by the relatively low C16 nitrile yield (6%) in the 60 min reference experiment, and high yields of the C16 amine (22%), C16 alcohol (22%) and C16 paraffin (12%). Pt/ZrO₂ was, consequently, the only catalyst that was more selective towards the C16 paraffin than the C15 paraffin in the tested conditions (Figure 5a).

The product sample of the 60 min reference experiment on Pt/ZrO₂ (Figure 4) additionally contained the C32 amine (9%), the C32 amide (7%) and the C32 ester (2%), which were converted to the C16 paraffin at higher batch residence times (Scheme 1, Figure 5a). The condensation reactions and competitive HDN and

HDO of the C16 amine and C16 alcohol characterized the reaction network of Pt/ZrO₂, as elaborated previously.^{27,28} Up to 10% of the C15 paraffin was formed via decarboxylation and decarbonylation routes on Pt/ZrO₂, but based on the batch residence time series (Figure 5a), the C–C bond hydrogenolysis of the C16 alcohol to the C15 paraffin was not favored. The pathway may have been more prominent on the metals which bind CH_x species stronger, such as Ru, Rh and Ni, as the selectivity between the C–O and C–C bond hydrogenolysis of alcohols has been found to depend on the relative ability of the metal to activate CH_x species.^{33,34,79–81} Lewis acid sites on the support (Figure 3b) and high H₂ pressures can inhibit decarbonylation reactions, which may have further contributed to why the conversion of the C16 alcohol to the C15 paraffin was not favorable on Pt/ZrO₂.^{5,81}

The enhanced C–O bond hydrogenolysis selectivity of Pt compared to Pd has been reported before and can be attributed to the metal properties, as Pd favors alkyl chain adsorption, while Pt may preferentially interact with carbonyl and hydroxyl functionalities.^{5,79,82–85} Stronger interactions between the active metal and the carbonyl group of the C16 amide may likewise explain why the C16 amide conversion was higher on Pt/ZrO₂ than on Pd/ZrO₂. However, a contribution of the differences in the surface composition and possibly the dispersion of the catalysts cannot be entirely excluded (Table 1, Table 2).

The product distribution of Ru/ZrO₂ and Rh/ZrO₂ shared similarities with each other and deviated from Ni/ZrO₂, Pd/ZrO₂ and Pt/ZrO₂. The highest paraffin yields in the hydrotreatment of the C16 amide were obtained on the Ru and Rh catalysts (Figure 4). Both catalysts readily produced the C15 paraffin, with yields of 39% and 30% for Ru/ZrO₂ and Rh/ZrO₂, respectively. With a conversion of 69%, Ru/ZrO₂ was more active than Rh/ZrO₂, which converted 59% of the C16 amide.

The product sample of the C16 amide hydrotreatment experiment on Rh/ZrO₂ did not contain C16 paraffin, and the total yield of the oxygen-containing intermediate products was only 3% (Figure 4). Together with the C15 paraffin yield, this highlights that Rh/ZrO₂ was highly active and selective for oxygen removal via C–C bond cleavage routes (Scheme 1). The enhanced Brønsted acid site concentration on Rh/ZrO₂ (Figure 3b) was thus not reflected in the product distribution, as Brønsted acid sites promote C–O and C–N hydrogenolysis routes.^{5,86} It is possible that the strong Lewis basic sites on the Rh catalyst (Figure 3a) facilitated the adsorption of carbonyl compounds, and thus enhanced the deoxygenation activity.^{5,87} Only traces of the C32 condensation products were found in the product sample of Rh/ZrO₂.

The C15 paraffin dominated the product distribution of Ru/ZrO₂ in the hydrotreatment of the C16 amide, but some C16 paraffin was formed additionally (Figure 5b). The C16 intermediates and the C32 condensation products were not formed on Ru/ZrO₂ to the same extent as on Pt/ZrO₂ (Figure 5a). Therefore, in sharp contrast to Pt/ZrO₂, the HDN and HDO of the C16 amide on Ru/ZrO₂ appeared to occur simultaneously or consecutively without significant desorption of the intermediates between the HDN and HDO steps (Figure 5b). Methane was found in the qualitative analysis of the gas phase sample of both Ru/ZrO₂ and Rh/ZrO₂, indicating methanation of the C1 compounds that were formed in parallel with the C15 paraffin.^{88,89} The formation of C_{n-1} paraffins out of C_n fatty acids has been proposed to occur through the splitting of a formic acid species on supported Pd catalysts.^{83,90} Similarly, the formation of the C15 paraffin through scission of a formamide type species from the C16 amide might be a possibility for Ru/ZrO₂ and Rh/ZrO₂. Due to the high deoxygenation activity of the catalysts and the thermal instability of formamide in the studied conditions, the favored C–C bond cleavage route could not be deduced from the activity test data.

The C–C bond cleavage activity of supported Ru and Rh catalysts has been demonstrated in the hydrotreatment of vegetable oils, fatty acids and alcohols,^{23,78,79} but to our knowledge, the selective C–C bond cleavage of fatty amides has not been reported before. Furthermore, with most amine hydrotreatment studies focusing on methylamine, information on the preference between C–C and C–N bond cleavage routes on reduced metal catalysts is limited. The hydrotreatment of the C16 amine was therefore studied separately.

3.3 Catalytic Hydrotreatment of 1-Hexadecylamine. Hydrotreatment experiments were carried out for the catalysts using the C16 amine as a model compound, in order to evaluate the HDN activity and the preference for C–N and C–C bond cleavage routes without the interference of simultaneous HDO. The experiments were carried out at 300 °C and 80 bar H₂, using a reaction time of 60 min. The products of the C16 amine hydrotreatment experiments were the C15 paraffin, the C16 paraffin, the C32 amine and traces of the C16 nitrile and the C16 alcohol. The product samples additionally contained isopropyl hexadecylamine (C19 amine), which likely was formed via a reaction between the C16 amine and acetone residues in the system (acetone was used to wash the reactor lines between the experiments). The C19 amine is not considered to be a true part of the C16 amine HDN reaction network and is therefore not discussed further. The product distribution, conversion and nitrogen removal of the

C16 amine experiments is shown in Figure 6. The reaction network for the hydrotreatment of the C16 amine is a part of the reaction network of the C16 amide (Scheme 1).

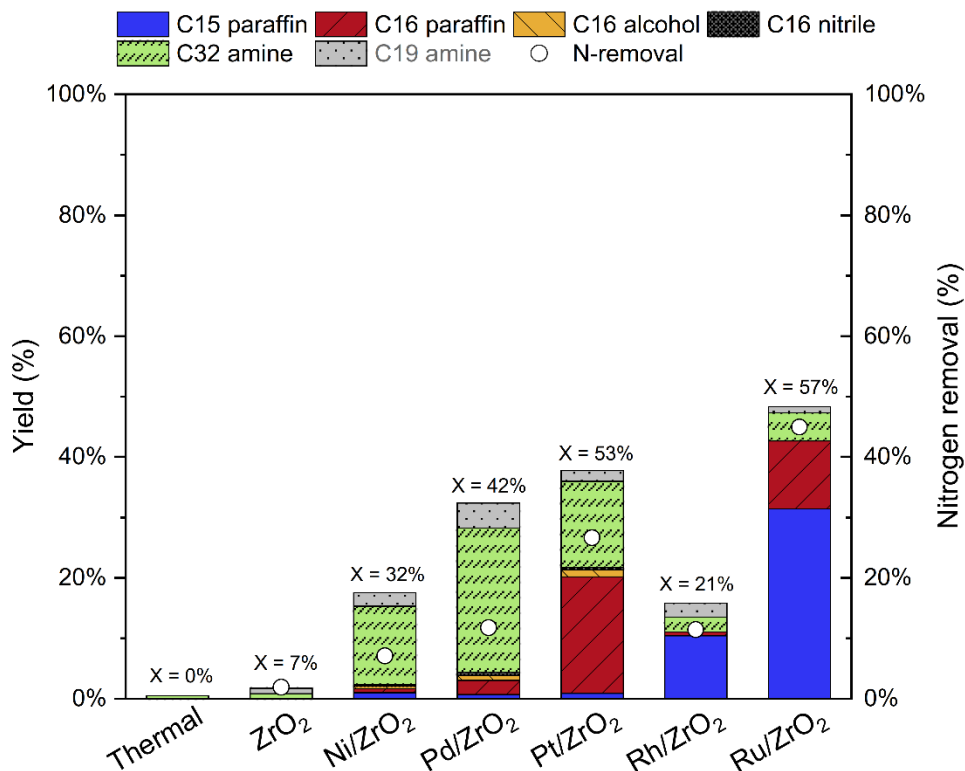


Figure 6. Product distribution, conversion and nitrogen removal (○) in the hydrotreatment of the C16 amine. The experiments were carried out at 300 °C and 80 bar H₂ for 60 min, stirring 600 rpm and using an initial nitrogen content of 100 ppm. The nitrogen removal was obtained from the total nitrogen content analysis.

The nitrogen removal in the 60 min C16 amine hydrotreatment experiments (Figure 6) increased in the order of ZrO₂ (1%) < Ni (7%) < Rh (11%), Pd (12%) << Pt (27%) << Ru (45%). A partly different ranking by HDN activity was thus obtained, and the variation in the nitrogen removal was considerably larger compared to the C16 amide hydrotreatment experiments (Figure 4) where the difference between the nitrogen removal of the most active and least active material was 25 percentage points. While all studied catalysts showed a lower activity in the hydrotreatment of the C16 amine than in the hydrotreatment of the C16 amide, the difference was particularly pronounced on Rh/ZrO₂, which removed 30 percentage points less nitrogen in the C16 amine experiment.

Batch residence time series experiments were carried out on the two most active catalysts, Pt/ZrO₂ and Ru/ZrO₂. Figure 7 displays the product distribution of Pt/ZrO₂ (a) and Ru/ZrO₂ (b) in the hydrotreatment of the C16 amine at 300 °C and 80 bar H₂, using 20 mg catalyst and an initial nitrogen content of 100 ppm. The 60 min reference experiments of Figure 6 correspond to the batch residence time 0.39 g_{cat}/g_{amine}. The following paragraphs discuss the activity and product distribution of the C16 amine hydrotreatment experiments on the catalysts.

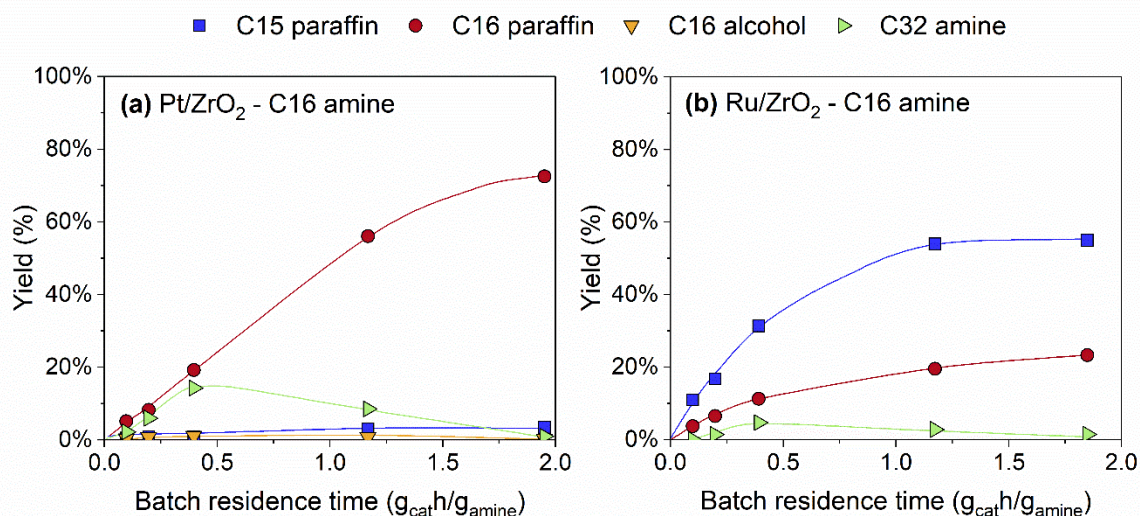


Figure 7. Product distribution as a function of batch residence time for (a) Pt/ZrO₂ and (b) Ru/ZrO₂ in the hydrotreatment of the C16 amine. The experiments were carried out at 300 °C, 80 bar H₂, using 20 mg of catalyst and an initial nitrogen content of 100 ppm. The trendlines have been added to guide the eye.

In contrast to the C16 amide hydrotreatment experiment (Figure 4), the ZrO₂ support showed a negligible nitrogen removal in the HDN of the C16 amine (Figure 6). The sites of ZrO₂ were therefore unable to catalyze reactions of the C16 amine in the tested conditions, which accounts for the lower conversion and nitrogen removal of the metal catalysts compared to the C16 amide experiments, where the support alone removed 28% nitrogen via BDA (Scheme 1). No thermal activity was recorded in the hydrotreatment of the C16 amine.

The C32 amine dominated the product distribution of Ni/ZrO₂ and Pd/ZrO₂ in the hydrotreatment of the C16 amine, with yields of 13% and 24%, respectively (Figure 6). The catalysts were therefore mainly active for the disproportionation of the C16 amine (Scheme 1).²⁵ The total paraffin yield of the C16 amine

experiments was less than 2% on Ni/ZrO₂ and 3% on Pd/ZrO₂, with Ni favoring the C15 paraffin and Pd favoring the C16 paraffin. The majority of the paraffins that were formed in the C16 amide experiments over Ni/ZrO₂ and Pd/ZrO₂ (Figure 4) therefore appeared to originate from the C16 acid, the C16 aldehyde or the C16 alcohol.

As with the C16 amide experiments (Figure 4), Pt/ZrO₂ exhibited the highest C16 paraffin yield (19%) out of the tested catalysts in the C16 amine hydrotreatment experiments (Figure 6). The C16 paraffin could be formed as a primary product in the hydrotreatment of the C16 amine on Pt/ZrO₂, which initially was reflected in higher C16 paraffin yields compared to a similar batch residence time with the C16 amide, despite a lower model compound conversion. The C16 to C15 paraffin ratio at the highest studied batch residence time was significantly higher in the hydrotreatment of the C16 amine (21.0 mol/mol, Figure 7a) compared to the hydrotreatment of the C16 amide (6.1 mol/mol, Figure 5a). The C–C bond cleavage of the C16 amine to the C15 paraffin did therefore not significantly occur on Pt/ZrO₂. This indicates that the C15 paraffin that was formed on Pt/ZrO₂ in the C16 amide experiments originated from decarbonylation and decarboxylation pathways (Scheme 1). The C16 paraffin and C32 amine yields were similar until batch residence time 0.39 g_{cat}h/g_{amine}.

Similar results have been reported previously for the activity of Pt and Pd in HDN. In their computational study, Almithn and Hibbis³³ found Pt to be more active than Pd for the C–N bond hydrogenolysis of methylamine, while Meitzner et al.²⁵ found that Pd was more selective for the disproportionation of methylamine to dimethylamine than Pt. In the 60 min C16 amine hydrotreatment experiments on Pd/ZrO₂ and Pt/ZrO₂, we obtained C32 amine to C16 paraffin ratios of 5 mol/mol and 0.4 mol/mol, respectively (Figure 6), which considering the higher reaction temperature and conversion level, aligns with the observations by Meitzner et al.²⁵ On the other hand, Ni has been predicted to be more active in C–N bond hydrogenolysis than both Pd and Pt.³³ It is possible that the low HDN activity of Ni/ZrO₂ was due to the poor Ni dispersion (Table 1) or incomplete reduction of Ni (Figure 1).

Interestingly, up to 2% of the C16 alcohol was found in the product samples of the C16 amine hydrotreatment experiments on Pt/ZrO₂ and Pd/ZrO₂ (Figure 6). The compound may have been formed using oxygen from the ZrO₂ surface. In a previous work by Verkama et al.,²⁸ the formation of alcohols from amines was observed on Pt/ZrO₂ in similar reaction conditions. Therefore, the conversion of the C16 amine to the C16 alcohol, and vice versa, likely occurred in the C16 amide experiments as well.⁹¹

The C15 paraffin was obtained as the main product in the C16 amine hydrotreatment experiments on Ru/ZrO₂ and Rh/ZrO₂, with yields of 31% and 10%, respectively (Figure 6). This confirms that Ru/ZrO₂ and Rh/ZrO₂ are active for the C–C bond cleavage of primary alkyl amines. Methane was found in the qualitative gas-phase analysis, but the absence of *n*-tetradecane (C14 paraffin) and other shorter chain paraffins in the product samples indicate that the C–C bond cleavage of the C16 amine to the C15 paraffin is more likely than cracking of the C16 paraffin to the C15 paraffin and methane. This is also supported by the batch residence time series experiments (Figure 5, Figure 7), where the paraffin yields did not decay over time. Di et al.⁷⁹ similarly found that Ru/TiO₂ catalyzed both the C–C and C–N bond hydrogenolysis of the C16 amine, and obtained methane as the exclusive carbon-containing gaseous product. The C32 amine yields were below 5% on both Ru/ZrO₂ and Rh/ZrO₂, in contrast to Pt/ZrO₂, Pd/ZrO₂ and Ni/ZrO₂, which favored the formation of the C32 amine.

Ru/ZrO₂ produced a C16 paraffin yield of 11% in the C16 amine experiment (Figure 6), which is higher than the C16 paraffin yield in the C16 amide experiments (Figure 4). This was also reflected in the batch residence time series experiments on Ru/ZrO₂, where C16 to C15 paraffin ratios of 0.4 mol/mol and 0.2 mol/mol were obtained at the highest batch residence time points for the C16 amine (Figure 7b) and C16 amide (Figure 5b), respectively. Ru/ZrO₂ was therefore less selective for the C–C bond cleavage of the C16 amine than for the C–C bond cleavage of the oxygen-containing compounds in the C16 amide reaction network (Scheme 1).

The product sample of the C16 amine hydrotreatment experiment on Rh/ZrO₂ did not contain C16 paraffin, which implies that Rh/ZrO₂ was the most selective catalyst for the C–C bond cleavage routes, regardless of its relatively low activity. Rh has been reported to exhibit a high activity for the C–N bond hydrogenolysis of methylamine to methane, which makes the low C16 amine conversion and complete lack of C16 paraffin in the C16 amine HDN experiments on Rh/ZrO₂ surprising, particularly considering that the C–C bond dissociation energy is higher than the C–N bond dissociation energy.^{25,29,33} Preferential interaction between the Rh sites and the alkyl chain, preventing the adsorption of the C16 amine in a favorable mode for C–N bond hydrogenolysis and stabilizing the transition states for the C–C bond cleavage route, might explain the selectivity of Rh/ZrO₂ in the hydrotreatment of the C16 amine. It is also possible that the relatively low concentration of Lewis acid sites (Figure 3b), strong basic sites (Figure 3a)

and electronic interactions between Rh and the support (Table S2, Supporting Information) influenced the catalytic properties of Rh/ZrO₂ in this context.

The mechanism for the formation of the C15 paraffin, the C16 paraffin and the C32 amine from the C16 amine cannot be confirmed from the experimental data, but it is likely that the reactions were initiated by the dissociative adsorption of the C16 amine as a hydrogen-deficient surface intermediate C₁₅H₃₁CH_xNH_y, and followed by a sequence of dehydrogenation, hydrogenation and C–C or C–N bond cleavage steps on the metal sites.^{25,29–34,80,92–94} The active metal influences the adsorption strength, preferred adsorption mode and transition states in the reaction mechanism, which can explain the differences in the activity and selectivity towards the different reaction pathways.^{25,29–34,80,92–94}

The activity of the metals of the groups 8-11 has been found to decrease from left to right in the periodic table, both in the case of C–C and C–N bond hydrogenolysis.^{25,29,33,95} While the amine group affects the reactivity of the adjacent C–C bond, the periodic trend for the activity towards C–C bond cleavage is reflected in the product distribution of the C16 amine experiments (Figure 6).^{33,95,96} In contrast, the periodic trend for the activity towards C–N bond cleavage only holds in the case of Pt/ZrO₂ and Pd/ZrO₂.^{25,33} This could indicate that the relative ability of the metals to activate CH_x species influenced the preference between C–C and C–N bond cleavage, similarly to what has been found in the hydrotreatment of alcohols.⁸¹

3.4 Comparison of the model compounds. Figure 8 presents the heteroatom removal in the hydrotreatment of the C16 amide and the C16 amine as a function of conversion for the catalysts and the ZrO₂ support. The data is from the 60 min reference experiments at 300 °C and 80 bar H₂ (Figure 4, Figure 6).

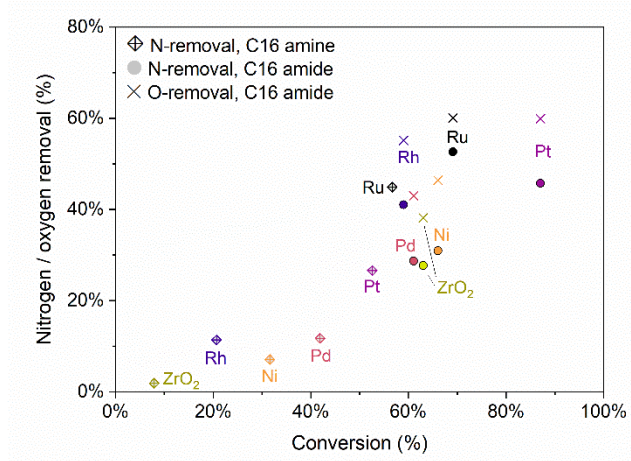


Figure 8. Heteroatom removal as a function of conversion in the hydrotreatment of the C16 amide and the C16 amine on the catalysts and the bare ZrO₂ support. Reaction conditions: 300 °C, 80 bar H₂, 60 min, 100 ppm initial N content, 20 mg catalyst.

The catalysts showed a higher conversion and nitrogen removal in the C16 amide hydrotreatment experiments than in the C16 amine hydrotreatment experiments (Figure 8), which can be explained by the activity of the ZrO₂ support for the conversion of the C16 amide via BDA (Scheme 1). Ru/ZrO₂ and Pt/ZrO₂ were the most active catalysts in terms of conversion and heteroatom removal in the hydrotreatment of both model compounds, but the order of activity varied for the other catalysts. While the initial conversion of the C16 amide to oxygen-containing and nitrogen-containing intermediate products proceeded efficiently, the further HDN of the nitrogen-containing intermediates was inhibited by the competitive HDO of the oxygen-containing intermediates.²⁸ The preference for HDO was reflected in a higher oxygen removal than nitrogen removal on the catalysts (Figure 4), and could also be observed from the product distribution of the batch residence time series experiments (Figure 5).

The interference of HDO may explain why the ranking of the catalysts by HDN activity differed in the C16 amide experiments and the C16 amine experiments (Figure 8). For example, the nitrogen removal of Pd/ZrO₂ was similar to the nitrogen removal of the bare ZrO₂ in the hydrotreatment of the C16 amide, even though Pd/ZrO₂ removed 11 percentage points more nitrogen than the bare ZrO₂ in the hydrotreatment of the C16 amine. The activity and preference for HDO was reflected in the product distribution, which indicated that Pd/ZrO₂ preferentially converted the oxygen-containing intermediates. The findings emphasize the relative complexity of the C16 amide reaction network and the interference

of competitive HDO and HDN reactions in the hydrotreatment of molecules which contain both oxygen and nitrogen.

The tested catalysts exhibited activity for the formation of the C15 paraffin via the decarboxylation and decarbonylation routes in the C16 amide reaction network (Scheme 1, Figure 4). Even Pt/ZrO₂, which was the least selective catalyst for C–C bond cleavage, produced 10% of the C15 paraffin at full conversion (Figure 5a). In contrast, only Ru/ZrO₂ and Rh/ZrO₂ displayed a significant activity for the C–C bond cleavage of the C16 amine (Figure 6, Figure 7b), and the C15 paraffin yields were lower than in the C16 amide experiments. The C–C bond cleavage of the oxygen-containing compounds in the reaction network therefore appeared to be more favorable than the C–C bond cleavage of the C16 amine on the studied catalysts, which aligns with the findings by Di et al.⁷⁹

4. Conclusions

In this work, ZrO₂-supported Pt, Pd, Rh, Ru and Ni catalysts were studied in the hydrotreatment of the C16 amide (*n*-hexadecanamide) and the C16 amine (1-hexadecylamine). Ru/ZrO₂ and Pt/ZrO₂ were the most active catalysts for the formation of *n*-paraffins from both model compounds, while Pd/ZrO₂ and Ni/ZrO₂ only displayed a modest activity at the studied reaction conditions.

The hydrotreatment of the C16 amide proceeded more efficiently than the hydrotreatment of the C16 amine on the studied catalysts, which was due to the activity of the ZrO₂ support for the conversion of the C16 amide. A high HDO activity was not always reflected in a high HDN activity. For example, Rh/ZrO₂ was highly active for oxygen removal via C–C bond cleavage routes in the C16 amide experiments, but only showed a low conversion and nitrogen removal in the HDN of the C16 amine.

The reaction network of the C16 amide was influenced both by the support and the activity and selectivity of the metals for the conversion of the oxygen-containing and nitrogen-containing intermediate products. The metal catalysts mainly differed in their tendency to catalyze condensation reactions and in their preference for C–C, C–O and C–N bond cleavage routes in the formation of the paraffins, which was reflected in the yields of the C32 condensation products, the C15 paraffin and the C16 paraffin. Characterization by CO and H₂ pulse chemisorption, XRD, XRF, CO₂-TPD, pyridine FTIR and N₂-physisorption could not explain the differences in the product distribution of the noble metal catalysts, which indicates that the metal identity and its influence on the adsorption strength, adsorption mode and transition states of the reactants and intermediate products accounted for the observed differences in the activity and selectivity. The low activity of the Ni/ZrO₂ catalyst may, however, have been due to the poor dispersion and/or incomplete reduction of Ni.

Ru/ZrO₂ and Rh/ZrO₂ were highly active for C–C bond cleavage routes and selectively formed the C15 paraffin in both the C16 amide and C16 amine hydrotreatment experiments. In case of the C16 amide, the C–C bond cleavage partly occurred from the oxygen-containing and nitrogen-containing intermediate products, but may also have occurred directly from the C16 amide. Pt/ZrO₂ was the only catalyst that was more selective for the formation of the C16 paraffin than the C15 paraffin from both model compounds, and the formation and decomposition of the C32 condensation products played an important role in reaction pathway towards the C16 paraffin. The C32 condensation products were likewise readily

produced by the low-activity Pd/ZrO₂ and Ni/ZrO₂ catalysts, whereas their formation was not preferred on Ru/ZrO₂ and Rh/ZrO₂, highlighting the mechanistic differences between the catalysts.

To our knowledge, the selective formation of C_{n-1} normal paraffins via C–C bond cleavage routes has not been reported before in the hydrotreatment of fatty amides and amines. The finding aligns with recent HDO studies over supported noble metal catalysts and emphasizes the influence of the active metal on the activity and selectivity of different supported noble metal catalysts.

Acknowledgement

Henni Kuokka is acknowledged for assistance with the batch reactor experiments. Dr. Hua Jiang and the facilities of the OtaNano Nanomicroscopy center are acknowledged for the STEM images. Dr. Yingnan Zhao and the Research Analytics department of Neste Corporation are acknowledged for the guidance and equipment support related to the pyridine FTIR measurements. This work used the Bioeconomy and Raw materials research infrastructures at Aalto University.

This work was funded by Neste Corporation as a part of the Neste-Aalto HDN catalyst development project.

Notes

Non-disclosure agreement prevents researchers from disclosing conflict of interest.

Supporting Information Available: Catalyst characterization data from N₂-physisorption, XRD, STEM and XPS measurements

References

- (1) Mortensen, P. M.; Grunwaldt, J.-D.; Jensen, P. A.; Knudsen, K. G.; Jensen, A. D. A Review of Catalytic Upgrading of Bio-Oil to Engine Fuels. *Appl. Catal., A* **2011**, *407*, 1–19. <https://doi.org/10.1016/j.apcata.2011.08.046>.
- (2) De, S.; Saha, B.; Luque, R. Hydrodeoxygenation Processes: Advances on Catalytic Transformations of Biomass-Derived Platform Chemicals into Hydrocarbon Fuels. *Bioresour. Technol.* **2015**, *178*, 108–118. <https://doi.org/10.1016/j.biortech.2014.09.065>.

- (3) Furimsky, E. Catalytic Hydrodeoxygenation. *Appl. Catal., A* **2000**, *199*, 147–190. [https://doi.org/10.1016/S0926-860X\(99\)00555-4](https://doi.org/10.1016/S0926-860X(99)00555-4).
- (4) Bu, Q.; Lei, H.; Zacher, A. H.; Wang, L.; Ren, S.; Liang, J.; Wei, Y.; Liu, Y.; Tang, J.; Zhang, Q.; Ruan, R. A Review of Catalytic Hydrodeoxygenation of Lignin-Derived Phenols from Biomass Pyrolysis. *Bioresour. Technol.* **2012**, *124*, 470–477. <https://doi.org/10.1016/j.biortech.2012.08.089>.
- (5) Ding, S.; Parlett, C. M. A.; Fan, X. Recent Developments in Multifunctional Catalysts for Fatty Acid Hydrodeoxygenation as a Route towards Biofuels. *Mol. Catal.* **2021**, *523*, 111492. <https://doi.org/10.1016/j.mcat.2021.111492>.
- (6) Rogers, K. A.; Zheng, Y. Selective Deoxygenation of Biomass-Derived Bio-Oils within Hydrogen-Modest Environments: A Review and New Insights. *ChemSusChem* **2016**, *9*, 1750–1772. <https://doi.org/10.1002/cssc.201600144>.
- (7) Huber, G. W.; O'Connor, P.; Corma, A. Processing Biomass in Conventional Oil Refineries: Production of High Quality Diesel by Hydrotreating Vegetable Oils in Heavy Vacuum Oil Mixtures. *Appl. Catal., A* **2007**, *329*, 120–129. <https://doi.org/10.1016/j.apcata.2007.07.002>.
- (8) Šimáček, P.; Kubička, D.; Šebor, G.; Pospíšil, M. Hydroprocessed Rapeseed Oil as a Source of Hydrocarbon-Based Biodiesel. *Fuel* **2009**, *88*, 456–460. <https://doi.org/10.1016/j.fuel.2008.10.022>.
- (9) Madl, T.; Mittelbach, M. Quantification of Primary Fatty Acid Amides in Commercial Tallow and Tallow Fatty Acid Methyl Esters by HPLC-APCI-MS. *Analyst* **2005**, *130*, 565–570. <https://doi.org/10.1039/b415779f>.
- (10) Palardy, O.; Behnke, C.; Laurens, L. M. L. Fatty Amide Determination in Neutral Molecular Fractions of Green Crude Hydrothermal Liquefaction Oils From Algal Biomass. *Energy Fuels* **2017**, *31*, 8275–8282. <https://doi.org/10.1021/acs.energyfuels.7b01175>.
- (11) Chen, W.-T.; Tang, L.; Qian, W.; Scheppe, K.; Nair, K.; Wu, Z.; Gai, C.; Zhang, P.; Zhang, Y. Extract Nitrogen-Containing Compounds in Biocrude Oil Converted from Wet Biowaste via Hydrothermal Liquefaction. *ACS Sustainable Chem. Eng.* **2016**, *4*, 2182–2190. <https://doi.org/10.1021/acssuschemeng.5b01645>.
- (12) Zimmermann, J.; Chiaberge, S.; Iversen, S. B.; Raffelt, K.; Dahmen, N. Sequential Extraction and Characterization of Nitrogen Compounds after Hydrothermal Liquefaction of Sewage Sludge. *Energy Fuels* **2022**, *36*, 14292–14303. <https://doi.org/10.1021/acs.energyfuels.2c02622>.
- (13) Batalha, N.; Checa, R.; Lorentz, C.; Afanasiev, P.; Stańczyk, K.; Kapusta, K.; Laurenti, D.; Geantet, C. Lignite and Biomass Waste Hydrothermal Liquefaction Crude Upgrading by Hydrotreatment. *Energy Fuels* **2023**, *37*, 10506–10520. <https://doi.org/10.1021/acs.energyfuels.3c01550>.

- (14) Heracleous, E.; Vassou, M.; Lappas, A. A.; Rodriguez, J. K.; Chiaberge, S.; Bianchi, D. Understanding the Upgrading of Sewage Sludge-Derived Hydrothermal Liquefaction Biocrude via Advanced Characterization. *Energy Fuels* **2022**, *36*, 12010–12020. <https://doi.org/10.1021/acs.energyfuels.2c01746>.
- (15) Furimsky, E.; Massoth, F. E. Hydrodenitrogenation of Petroleum. *Catal. Rev.* **2005**, *47*, 297–489. <https://doi.org/10.1081/CR-200057492>.
- (16) Castello, D.; Haider, M. S.; Rosendahl, L. A. Catalytic Upgrading of Hydrothermal Liquefaction Biocrudes: Different Challenges for Different Feedstocks. *Renew. Energy* **2019**, *141*, 420–430. <https://doi.org/10.1016/j.renene.2019.04.003>.
- (17) Li, Z.; Savage, P. E. Feedstocks for Fuels and Chemicals from Algae: Treatment of Crude Bio-Oil over HZSM-5. *Algal Res.* **2013**, *2*, 154–163. <https://doi.org/10.1016/j.algal.2013.01.003>.
- (18) López Barreiro, D.; Gómez, B. R.; Ronsse, F.; Hornung, U.; Kruse, A.; Prins, W. Heterogeneous Catalytic Upgrading of Biocrude Oil Produced by Hydrothermal Liquefaction of Microalgae: State of the Art and Own Experiments. *Fuel Process. Technol.* **2016**, *148*, 117–127. <https://doi.org/10.1016/j.fuproc.2016.02.034>.
- (19) Biller, P.; Sharma, B. K.; Kunwar, B.; Ross, A. B. Hydroprocessing of Bio-Crude from Continuous Hydrothermal Liquefaction of Microalgae. *Fuel* **2015**, *159*, 197–205. <https://doi.org/10.1016/j.fuel.2015.06.077>.
- (20) Zhu, C.; Gutiérrez, O. Y.; Santosa, D. M.; Flake, M.; Weindl, R.; Kutnyakov, I.; Shi, H.; Wang, H. Kinetics of Nitrogen-, Oxygen- and Sulfur-Containing Compounds Hydrotreating during Co-Processing of Bio-Crude with Petroleum Stream. *Appl. Catal., B* **2022**, *307*, 121197. <https://doi.org/10.1016/j.apcatb.2022.121197>.
- (21) Liu, M.; Shi, Y.; Wu, K.; Liang, J.; Wu, Y.; Huang, S.; Yang, M. Upgrading of Palmitic Acid and Hexadecanamide over Co-Based Catalysts: Effect of Support (SiO₂, γ-Al₂O₃ and H-ZSM-22). *Catal. Commun.* **2019**, *129*, 105726. <https://doi.org/10.1016/j.catcom.2019.105726>.
- (22) Snåre, M.; Kubičková, I.; Mäki-Arvela, P.; Eränen, K.; Murzin, D. Yu. Heterogeneous Catalytic Deoxygenation of Stearic Acid for Production of Biodiesel. *Ind. Eng. Chem. Res.* **2006**, *45*, 5708–5715. <https://doi.org/10.1021/ie060334i>.
- (23) Malins, K. Synthesis of Renewable Hydrocarbons from Vegetable Oil Feedstock by Hydrotreatment over Selective Sulfur-Free SiO₂-Al₂O₃ Supported Monometallic Pd, Pt, Ru, Ni, Mo and Bimetallic NiMo Catalysts. *Fuel* **2021**, *285*, 119129. <https://doi.org/10.1016/j.fuel.2020.119129>.

- (24) Furimsky, E. Hydroprocessing Challenges in Biofuels Production. *Catal. Today* **2013**, *217*, 13–56. <https://doi.org/10.1016/j.cattod.2012.11.008>.
- (25) Meitzner, G. Metal-Catalyzed Reactions of Methylamine in the Presence of Hydrogen. *J. Catal.* **1986**, *98*, 513–521. [https://doi.org/10.1016/0021-9517\(86\)90339-8](https://doi.org/10.1016/0021-9517(86)90339-8).
- (26) Marafi, M.; Furimsky, E. Hydroprocessing Catalysts Containing Noble Metals: Deactivation, Regeneration, Metals Reclamation, and Environment and Safety. *Energy Fuels* **2017**, *31*, 5711–5750. <https://doi.org/10.1021/acs.energyfuels.7b00471>.
- (27) Verkama, E.; Albersberger, S.; Arandia, A.; Meinander, K.; Tiitta, M.; Karinen, R.; Puurunen, R. L. Hydrodeoxygenation and Hydrodenitrogenation of *n*-Hexadecanamide over Pt Catalysts: Effect of the Support. Preprint **2023**. <https://doi.org/10.26434/chemrxiv-2023-9nzcq>
- (28) Verkama, E.; Auvinen, P.; Albersberger, S.; Tiitta, M.; Karinen, R.; Puurunen, R. L. Competitive Hydrodeoxygenation and Hydrodenitrogenation Reactions in the Hydrotreatment of Fatty Acid and Amine Mixtures. *Top. Catal.* **2023**, *66*, 1353–1368. <https://doi.org/10.1007/s11244-023-01784-w>.
- (29) Meitzner, G.; Mykytka, W. J.; Sinfelt, J. H. Kinetics of Hydrogenolysis of Methylamine on a Rhodium Catalyst. *Catal. Lett.* **1995**, *32*, 335–344. <https://doi.org/10.1007/BF00813228>.
- (30) Migone, R. A.; Meitzner, G.; Mykytka, W. J.; Sinfelt, J. H. Kinetics of Methylamine Conversion on a Pd Catalyst in the Presence of H₂. *Catal. Lett.* **1995**, *31*, 27–35. <https://doi.org/10.1007/BF00817030>.
- (31) Sinfelt, J. H. Catalytic Hydrogenolysis on Metals. *Catal. Lett.* **1991**, *9*, 159–171. <https://doi.org/10.1007/BF00773174>.
- (32) Cattenot, M.; Peeters, E.; Geantet, C.; Devers, E.; Zotin, J. L. Mechanism of Carbon–Nitrogen Bond Scission in the Presence of H₂S on Pt Supported Catalysts. *Catal. Lett.* **2005**, *99*, 171–176. <https://doi.org/10.1007/s10562-005-2110-z>.
- (33) Almithn, A. S.; Hibbitts, D. D. Impact of Metal and Heteroatom Identities in the Hydrogenolysis of C–X Bonds (X = C, N, O, S, and Cl). *ACS Catal.* **2020**, *10*, 5086–5100. <https://doi.org/10.1021/acscatal.0c00481>.
- (34) Li, M.-R.; Wang, G.-C. Differentiation of the C–O and C–C Bond Scission Mechanisms of 1-Hexadecanol on Pt(111) and Ru(0001): A First Principles Analysis. *Catal. Sci. Technol.* **2017**, *7*, 743–760. <https://doi.org/10.1039/C6CY02529C>.
- (35) Kon, K.; Onodera, W.; Takakusagi, S.; Shimizu, K. Hydrodeoxygenation of Fatty Acids and Triglycerides by Pt-Loaded Nb₂O₅ Catalysts. *Catal. Sci. Technol.* **2014**, *4*, 3705–3712. <https://doi.org/10.1039/C4CY00757C>.

- (36) Bie, Y.; Lehtonen, J.; Kanervo, J. Hydrodeoxygenation (HDO) of Methyl Palmitate over Bifunctional Rh/ZrO₂ Catalyst: Insights into Reaction Mechanism via Kinetic Modeling. *Appl. Catal., A* **2016**, *526*, 183–190. <https://doi.org/10.1016/j.apcata.2016.08.030>.
- (37) Ni, J.; Leng, W.; Mao, J.; Wang, J.; Lin, J.; Jiang, D.; Li, X. Tuning Electron Density of Metal Nickel by Support Defects in Ni/ZrO₂ for Selective Hydrogenation of Fatty Acids to Alkanes and Alcohols. *Appl. Catal., B* **2019**, *253*, 170–178. <https://doi.org/10.1016/j.apcatb.2019.04.043>.
- (38) Biller, P.; Ross, A. B. Potential Yields and Properties of Oil from the Hydrothermal Liquefaction of Microalgae with Different Biochemical Content. *Bioresour. Technol.* **2011**, *102*, 215–225. <https://doi.org/10.1016/j.biortech.2010.06.028>.
- (39) Brunauer, S.; Emmett, P. H.; Teller, E. Adsorption of Gases in Multimolecular Layers. *J. Am. Chem. Soc.* **1938**, *60*, 309–319. <https://doi.org/10.1021/ja01269a023>.
- (40) Barrett, E. P.; Joyner, L. G.; Halenda, P. P. The Determination of Pore Volume and Area Distributions in Porous Substances. I. Computations from Nitrogen Isotherms. *J. Am. Chem. Soc.* **1951**, *73*, 373–380. <https://doi.org/10.1021/ja01145a126>.
- (41) Bergeret, G.; Gallezot, P. Particle Size and Dispersion Measurements. In *Handbook of Heterogeneous Catalysis*; John Wiley & Sons, Ltd, 2008; pp 738–765. <https://doi.org/10.1002/9783527610044.hetcat0038>.
- (42) Powell, C. X-Ray Photoelectron Spectroscopy Database XPS, Version 4.1, NIST Standard Reference Database 20, 1989. <https://doi.org/10.18434/T4T88K>.
- (43) Emeis, C. A. Determination of Integrated Molar Extinction Coefficients for Infrared Absorption Bands of Pyridine Adsorbed on Solid Acid Catalysts. *J. Catal.* **1993**, *141*, 347–354. <https://doi.org/10.1006/jcat.1993.1145>.
- (44) de Saint Laumer, J.-Y.; Cicchetti, E.; Merle, P.; Egger, J.; Chaintreau, A. Quantification in Gas Chromatography: Prediction of Flame Ionization Detector Response Factors from Combustion Enthalpies and Molecular Structures. *Anal. Chem.* **2010**, *82*, 6457–6462. <https://doi.org/10.1021/ac1006574>.
- (45) Thommes, M.; Kaneko, K.; Neimark, A. V.; Olivier, J. P.; Rodriguez-Reinoso, F.; Rouquerol, J.; Sing, K. S. W. Physisorption of Gases, with Special Reference to the Evaluation of Surface Area and Pore Size Distribution (IUPAC Technical Report). *Pure Appl. Chem.* **2015**, *87*, 1051–1069. <https://doi.org/10.1515/pac-2014-1117>.

- (46) Behrens, M.; Schlögl, R. X-Ray Diffraction and Small Angle X-Ray Scattering. In *Characterization of Solid Materials and Heterogeneous Catalysts*; 2012; pp 609–653. <https://doi.org/10.1002/9783527645329.ch15>.
- (47) Jia, X.; Zhang, X.; Rui, N.; Hu, X.; Liu, C. Structural Effect of Ni/ZrO₂ Catalyst on CO₂ Methanation with Enhanced Activity. *Appl. Catal., B* **2019**, *244*, 159–169. <https://doi.org/10.1016/j.apcatb.2018.11.024>.
- (48) Tsiotsias, A. I.; Hafeez, S.; Charisiou, N. D.; Al-Salem, S. M.; Manos, G.; Constantinou, A.; AlKhoori, S.; Sebastian, V.; Hinder, S. J.; Baker, M. A.; Polychronopoulou, K.; Goula, M. A. Selective Catalytic Deoxygenation of Palm Oil to Produce Green Diesel over Ni Catalysts Supported on ZrO₂ and CeO₂–ZrO₂: Experimental and Process Simulation Modelling Studies. *Renew. Energy* **2023**, *206*, 582–596. <https://doi.org/10.1016/j.renene.2023.02.038>.
- (49) Italiano, C.; Llorca, J.; Pino, L.; Ferraro, M.; Antonucci, V.; Vita, A. CO and CO₂ Methanation over Ni Catalysts Supported on CeO₂, Al₂O₃ and Y₂O₃ Oxides. *Appl. Catal., B* **2020**, *264*, 118494. <https://doi.org/10.1016/j.apcatb.2019.118494>.
- (50) Omarov, Sh. O.; Sladkovskiy, D. A.; Martinson, K. D.; Peurla, M.; Aho, A.; Murzin, D. Yu.; Popkov, V. I. Influence of the Initial State of ZrO₂ on Genesis, Activity and Stability of Ni/ZrO₂ Catalysts for Steam Reforming of Glycerol. *Appl. Catal., A* **2021**, *616*, 118098. <https://doi.org/10.1016/j.apcata.2021.118098>.
- (51) Batista, J.; Pintar, A.; Mandrino, D.; Jenko, M.; Martin, V. XPS and TPR Examinations of γ -Alumina-Supported Pd-Cu Catalysts. *Appl. Catal., A* **2001** *206*, 113–124. [https://doi.org/10.1016/S0926-860X\(00\)00589-5](https://doi.org/10.1016/S0926-860X(00)00589-5)
- (52) Mäkelä, E.; Escobedo, J. L. G.; Neuvonen, J.; Lahtinen, J.; Lindblad, M.; Lassi, U.; Karinen, R.; Puurunen, R. L. Liquid-Phase Hydrodeoxygenation of 4-Propylphenol to Propylbenzene: Reducible Supports for Pt Catalysts. *ChemCatChem* **2020**, *12*, 4090–4104. <https://doi.org/10.1002/cctc.202000429>.
- (53) Hoang, D. L.; Lieske, H. Effect of Hydrogen Treatments on ZrO₂ and Pt/ZrO₂ Catalysts. *Catal. Lett.* **1994**, *27*, 33–42. <https://doi.org/10.1007/BF00806975>.
- (54) Wang, J. A.; López, T.; Bokhimi, X.; Novaro, O. Phase Composition, Reducibility and Catalytic Activity of Rh/Zirconia and Rh/Zirconia-Ceria Catalysts. *J. Mol. Catal. A: Chem.* **2005**, *239*, 249–256. <https://doi.org/10.1016/j.molcata.2005.06.021>.
- (55) Fornasiero, P.; Dimonte, R.; Rao, G. R.; Kaspar, J.; Meriani, S.; Trovarelli, A.; Graziani, M. Rh-Loaded CeO₂-ZrO₂ Solid-Solutions as Highly Efficient Oxygen Exchangers: Dependence of the Reduction

- Behavior and the Oxygen Storage Capacity on the Structural-Properties. *J. Catal.* **1995**, *151*, 168–177. <https://doi.org/10.1006/jcat.1995.1019>.
- (56) Eriksson, S.; Rojas, S.; Boutonnet, M.; Fierro, J. L. G. Effect of Ce-Doping on Rh/ZrO₂ Catalysts for Partial Oxidation of Methane. *Appl. Catal., A* **2007**, *326*, 8–16. <https://doi.org/10.1016/j.apcata.2007.03.019>.
- (57) Coq, B.; Kumbhar, P. S.; Moreau, C.; Moreau, P.; Figueras, F. Zirconia-Supported Monometallic Ru and Bimetallic Ru-Sn, Ru-Fe Catalysts: Role of Metal Support Interaction in the Hydrogenation of Cinnamaldehyde. *J. Phys. Chem.* **1994**, *98*, 10180–10188. <https://doi.org/10.1021/j100091a038>.
- (58) Józwiak, W. K. Influence of Reoxidation Temperature on TPR of Zirconia Supported Rhodium. *React Kinet Catal. Lett.* **1986**, *30*, 345–351. <https://doi.org/10.1007/BF02064312>.
- (59) Mohamed, Z.; Dasireddy, V. D. B. C.; Singh, S.; Friedrich, H. B. TiO₂ and ZrO₂ Supported Ru Catalysts for CO Mitigation Following the Water-Gas Shift Reaction. *Int. J. Hydrogen Energy* **2018**, *43*, 22291–22302. <https://doi.org/10.1016/j.ijhydene.2018.10.061>.
- (60) Wei, H.; Yan, X.; He, S.; Sun, C. Catalytic Wet Air Oxidation of Pentachlorophenol over Ru/ZrO₂ and Ru/ZrSiO₂ Catalysts. *Catal. Today* **2013**, *201*, 49–56. <https://doi.org/10.1016/j.cattod.2012.07.004>.
- (61) Choque, V.; de la Piscina, P. R.; Molyneux, D.; Homs, N. Ruthenium Supported on New TiO₂–ZrO₂ Systems as Catalysts for the Partial Oxidation of Methane. *Catal. Today* **2010**, *149*, 248–253. <https://doi.org/10.1016/j.cattod.2009.09.017>.
- (62) Valdés-Martínez, O. U.; Díaz de León, J. N.; Santolalla, C. E.; Talavera-López, A.; Avila-Paredes, H.; de los Reyes, J. A. Fundamental Study of Catalytic Functionalities Involved in Effective C–O Cleavage over Ru-Supported Catalysts. *Ind. Eng. Chem. Res.* **2021**, *60*, 18880–18890. <https://doi.org/10.1021/acs.iecr.1c03058>.
- (63) Viinikainen, T.; Rönkkönen, H.; Bradshaw, H.; Stephenson, H.; Airaksinen, S.; Reinikainen, M.; Simell, P.; Krause, O. Acidic and Basic Surface Sites of Zirconia-Based Biomass Gasification Gas Clean-up Catalysts. *Appl. Catal., A* **2009**, *362*, 169–177. <https://doi.org/10.1016/j.apcata.2009.04.037>.
- (64) Vo, D.-V. N.; Adesina, A. A. A Potassium-Promoted Mo Carbide Catalyst System for Hydrocarbon Synthesis. *Catal. Sci. Technol.* **2012**, *2*, 2066–2076. <https://doi.org/10.1039/C2CY20385E>.
- (65) Busca, G. The Surface Acidity of Solid Oxides and Its Characterization by IR Spectroscopic Methods. An Attempt at Systematization. *Phys. Chem. Chem. Phys.* **1999**, *1*, 723–736. <https://doi.org/10.1039/A808366E>.
- (66) Tamura, M.; Shimizu, K.; Satsuma, A. Comprehensive IR Study on Acid/Base Properties of Metal Oxides. *Appl. Catal., A* **2012**, *433–434*, 135–145. <https://doi.org/10.1016/j.apcata.2012.05.008>.

- (67) Wu, P.; Tang, X.; He, Z.; Liu, Y.; Wang, Z. Alkali Metal Poisoning and Regeneration of Selective Catalytic Reduction Denitration Catalysts: Recent Advances and Future Perspectives. *Energy Fuels* **2022**, *36*, 5622–5646. <https://doi.org/10.1021/acs.energyfuels.2c01036>.
- (68) Davidson, D.; Karten, M. The Pyrolysis of Amides. *J. Am. Chem. Soc.* **1956**, *78*, 1066–1068. <https://doi.org/10.1021/ja01586a051>.
- (69) Cabrero-Antonino, J. R.; Adam, R.; Papa, V.; Beller, M. Homogeneous and Heterogeneous Catalytic Reduction of Amides and Related Compounds Using Molecular Hydrogen. *Nat. Commun.* **2020**, *11*, 3893. <https://doi.org/10.1038/s41467-020-17588-5>.
- (70) Pestman, R.; van Duijne, A.; Pieterse, J. A. Z.; Ponec, V. The Formation of Ketones and Aldehydes from Carboxylic Acids, Structure-Activity Relationship for Two Competitive Reactions. *J. Mol. Catal. A: Chem.* **1995**, *103*, 175–180. [https://doi.org/10.1016/1381-1169\(95\)00138-7](https://doi.org/10.1016/1381-1169(95)00138-7).
- (71) Pestman, R.; Koster, R. M.; Pieterse, J. A. Z.; Ponec, V. Reactions of Carboxylic Acids on Oxides: 1. Selective Hydrogenation of Acetic Acid to Acetaldehyde. *J. Catal.* **1997**, *168*, 255–264. <https://doi.org/10.1006/jcat.1997.1623>.
- (72) Pestman, R.; Koster, R. M.; van Duijne, A.; Pieterse, J. A. Z.; Ponec, V. Reactions of Carboxylic Acids on Oxides: 2. Bimolecular Reaction of Aliphatic Acids to Ketones. *J. Catal.* **1997**, *168*, 265–272. <https://doi.org/10.1006/jcat.1997.1624>.
- (73) Salvatore, R. N.; Yoon, C. H.; Jung, K. W. Synthesis of Secondary Amines. *Tetrahedron* **2001**, *57*, 7785–7811. [https://doi.org/10.1016/S0040-4020\(01\)00722-0](https://doi.org/10.1016/S0040-4020(01)00722-0)
- (74) Greenfield, H. Catalytic Hydrogenation of Butyronitrile. *Ind. Eng. Chem. Prod. Res. Dev.* **1967**, *6*, 142–144. <https://doi.org/10.1021/i360022a014>.
- (75) Adamczyk, A. J. First-Principles Analysis of Acetonitrile Reaction Pathways to Primary, Secondary, and Tertiary Amines on Pd(111). *Surf. Sci.* **2019**, *682*, 84–98. <https://doi.org/10.1016/j.susc.2018.09.006>.
- (76) Sivasankar, N.; Prins, R. Reactions of Mixed Dialkyl- and Trialkylamines over Pd/ γ -Al₂O₃. *J. Catal.* **2006**, *241*, 342–355. <https://doi.org/10.1016/j.jcat.2006.04.032>.
- (77) Peng, B.; Zhao, C.; Kasakov, S.; Foraita, S.; Lercher, J. A. Manipulating Catalytic Pathways: Deoxygenation of Palmitic Acid on Multifunctional Catalysts. *Chem. Eur. J.* **2013**, *19*, 4732–4741. <https://doi.org/10.1002/chem.201203110>.
- (78) Malins, K.; Malina, I. The Effects of Supported Pd, Pt, Re, Rh, Ru, Ir, Au, and Ni Catalysts on Renewable Hydrocarbon Production from Alternative Feedstock. *Biomass Bioenergy* **2023**, *171*, 106732. <https://doi.org/10.1016/j.biombioe.2023.106732>.

- (79) Di, L.; Yao, S.; Li, M.; Wu, G.; Dai, W.; Wang, G.; Li, L.; Guan, N. Selective Catalytic Hydrogenolysis of Carbon–Carbon σ Bonds in Primary Aliphatic Alcohols over Supported Metals. *ACS Catal.* **2015**, *5*, 7199–7207. <https://doi.org/10.1021/acscatal.5b02180>.
- (80) Sutton, J. E.; Vlachos, D. G. Ethanol Activation on Closed-Packed Surfaces. *Ind. Eng. Chem. Res.* **2015**, *54*, 4213–4225. <https://doi.org/10.1021/ie5043374>.
- (81) Gürbüz, E. I.; Hibbitts, D. D.; Iglesia, E. Kinetic and Mechanistic Assessment of Alkanol/Alkanal Decarbonylation and Deoxygenation Pathways on Metal Catalysts. *J. Am. Chem. Soc.* **2015**, *137*, 11984–11995. <https://doi.org/10.1021/jacs.5b05361>.
- (82) Bhogeswararao, S.; Srinivas, D. Catalytic Conversion of Furfural to Industrial Chemicals over Supported Pt and Pd Catalysts. *J. Catal.* **2015**, *327*, 65–77. <https://doi.org/10.1016/j.jcat.2015.04.018>.
- (83) Boda, L.; Onyestyák, G.; Solt, H.; Lónyi, F.; Valyon, J.; Thernes, A. Catalytic Hydroconversion of Tricaprylin and Caprylic Acid as Model Reaction for Biofuel Production from Triglycerides. *Appl. Catal., A* **2010**, *374*, 158–169. <https://doi.org/10.1016/j.apcata.2009.12.005>.
- (84) Veriansyah, B.; Han, J. Y.; Kim, S. K.; Hong, S.-A.; Kim, Y. J.; Lim, J. S.; Shu, Y.-W.; Oh, S.-G.; Kim, J. Production of Renewable Diesel by Hydroprocessing of Soybean Oil: Effect of Catalysts. *Fuel* **2012**, *94*, 578–585. <https://doi.org/10.1016/j.fuel.2011.10.057>.
- (85) Delbecq, F.; Sautet, P. Competitive C=C and C=O Adsorption of α - β -Unsaturated Aldehydes on Pt and Pd Surfaces in Relation with the Selectivity of Hydrogenation Reactions: A Theoretical Approach. *J. Catal.* **1995**, *152*, 217–236. <https://doi.org/10.1006/jcat.1995.1077>.
- (86) Farneth, W. E.; Gorte, R. J. Methods for Characterizing Zeolite Acidity. *Chem. Rev.* **1995**, *95*, 615–635. <https://doi.org/10.1021/cr00035a007>.
- (87) Li, J.; Zhang, J.; Wang, S.; Xu, G.; Wang, H.; Vlachos, D. G. Chemoselective Hydrodeoxygenation of Carboxylic Acids to Hydrocarbons over Nitrogen-Doped Carbon–Alumina Hybrid Supported Iron Catalysts. *ACS Catal.* **2019**, *9*, 1564–1577. <https://doi.org/10.1021/acscatal.8b04967>.
- (88) Mills, G. A.; Steffgen, F. W. Catalytic Methanation. *Catal. Rev.* **1974**, *8*, 159–210. <https://doi.org/10.1080/01614947408071860>.
- (89) Gao, J.; Liu, Q.; Gu, F.; Liu, B.; Zhong, Z.; Su, F. Recent Advances in Methanation Catalysts for the Production of Synthetic Natural Gas. *RSC Adv.* **2015**, *5*, 22759–22776. <https://doi.org/10.1039/C4RA16114A>.
- (90) Berenblyum, A. S.; Danyushevsky, V. Ya.; Katsman, E. A.; Podoplelova, T. A.; Flid, V. R. Production of Engine Fuels from Inedible Vegetable Oils and Fats. *Pet. Chem.* **2010**, *50*, 305–311. <https://doi.org/10.1134/S0965544110040080>.

- (91) Coeck, R.; Berden, S.; Vos, D. E. D. Sustainable Hydrogenation of Aliphatic Acyclic Primary Amides to Primary Amines with Recyclable Heterogeneous Ruthenium–Tungsten Catalysts. *Green Chem.* **2019**, *21*, 5326–5335. <https://doi.org/10.1039/C9GC01310E>.
- (92) Johnson, D. F.; Wang, Y.; Parmeter, J. E.; Hills, M. M.; Weinberg, W. H. Chemisorption and Thermal Decomposition of Methylamine on the Ruthenium(001) Surface. *J. Am. Chem. Soc.* **1992**, *114*, 4279–4290. <https://doi.org/10.1021/ja00037a036>.
- (93) Lv, C.-Q.; Li, J.; Ling, K.-C.; Shang, Z.-F.; Wang, G.-C. Methylamine Decomposition on Nickel Surfaces: A Density Functional Theory Study. *Surf. Sci.* **2010**, *604*, 779–787. <https://doi.org/10.1016/j.susc.2010.01.027>.
- (94) Hwang, S. Y.; Kong, A. C. F.; Schmidt, L. D. Surface Chemistry of Carbon-Nitrogen Bonds on Rhodium(111). 1. Ethanedinitrile and Methylamine. *J. Phys. Chem.* **1989**, *93*, 8327–8333. <https://doi.org/10.1021/j100363a011>.
- (95) Sinfelt, J. H. Specificity in Catalytic Hydrogenolysis by Metals. In *Advances in Catalysis*; Eley, D. D., Pines, H., Weisz, P. B., Eds.; Academic Press, 1973; Vol. 23, pp 91–119. [https://doi.org/10.1016/S0360-0564\(08\)60299-0](https://doi.org/10.1016/S0360-0564(08)60299-0).
- (96) Sinfelt, J. H.; Yates, D. J. C. Catalytic Hydrogenolysis of Ethane over the Noble Metals of Group VIII. *J. Catal.* **1967**, *8*, 82–90. [https://doi.org/10.1016/0021-9517\(67\)90284-9](https://doi.org/10.1016/0021-9517(67)90284-9).

Supporting Information: Zirconia-supported Pt, Pd, Rh, Ru and Ni Catalysts in the Hydrotreatment of Fatty Amides and Amines

Emma Verkama^{1*}, Sylvia Albersberger², Kristoffer Meinander³, Marja Tiitta^{2†}, Reetta Karinen¹, Riikka L. Puurunen¹

¹Department of Chemical and Metallurgical Engineering, School of Chemical Engineering, Aalto University, P.O. Box 16100, 00076 Aalto, Finland

²Neste Corporation, P.O. Box 310, 06101 Porvoo, Finland

³Department of Bioproducts and Biosystems, School of Chemical Engineering, Aalto University, P.O. Box 16300, 00076 Aalto, Finland

Present address:

†Hamari, Finland

* Corresponding author:

Email: emma.verkama@aalto.fi

N₂-Physisorption Isotherms and Pore Size Distribution

Figure S1 displays the N₂-physisorption isotherms of the catalysts and the bare ZrO₂ support.

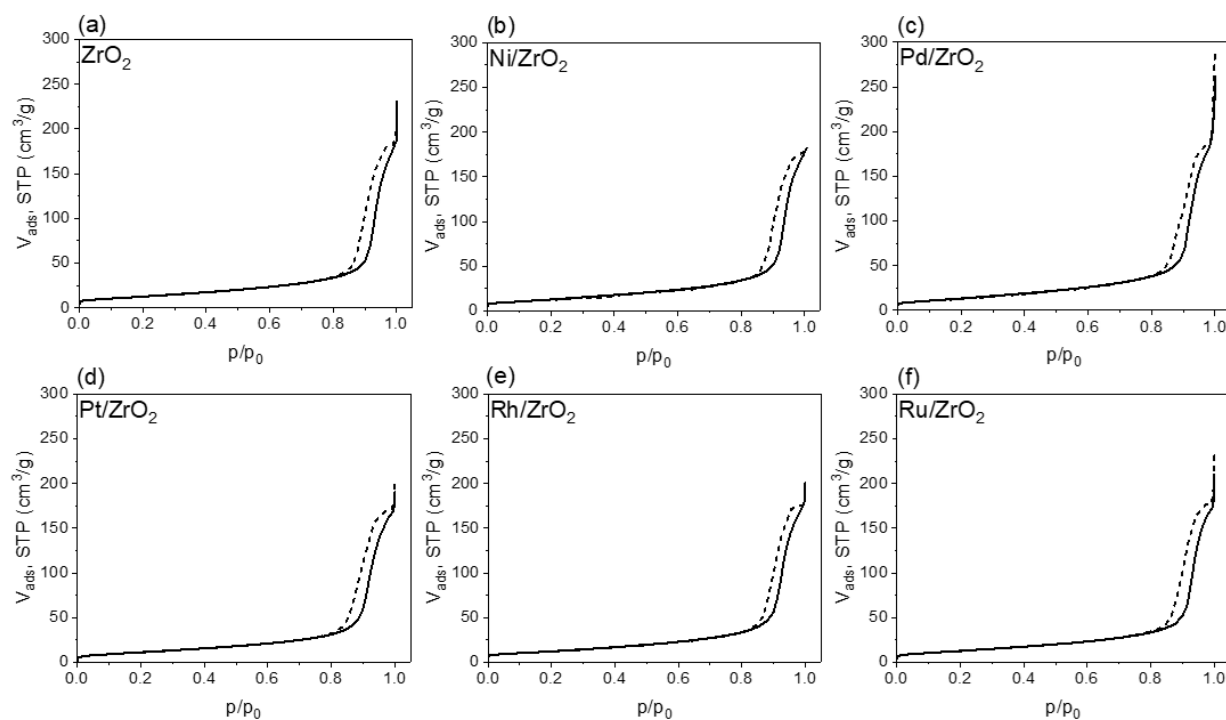


Figure S1. N₂-physisorption isotherms of (a) the bare ZrO₂ support and the calcined (b) Ni/ZrO₂, (c) Pd/ZrO₂, (d) Pt/ZrO₂, (e) Rh/ZrO₂ and (f) Ru/ZrO₂ catalysts.

Figure S2 displays the Barrett-Joyner-Halenda (BJH) pore size distribution of the catalysts and the bare ZrO₂ support.

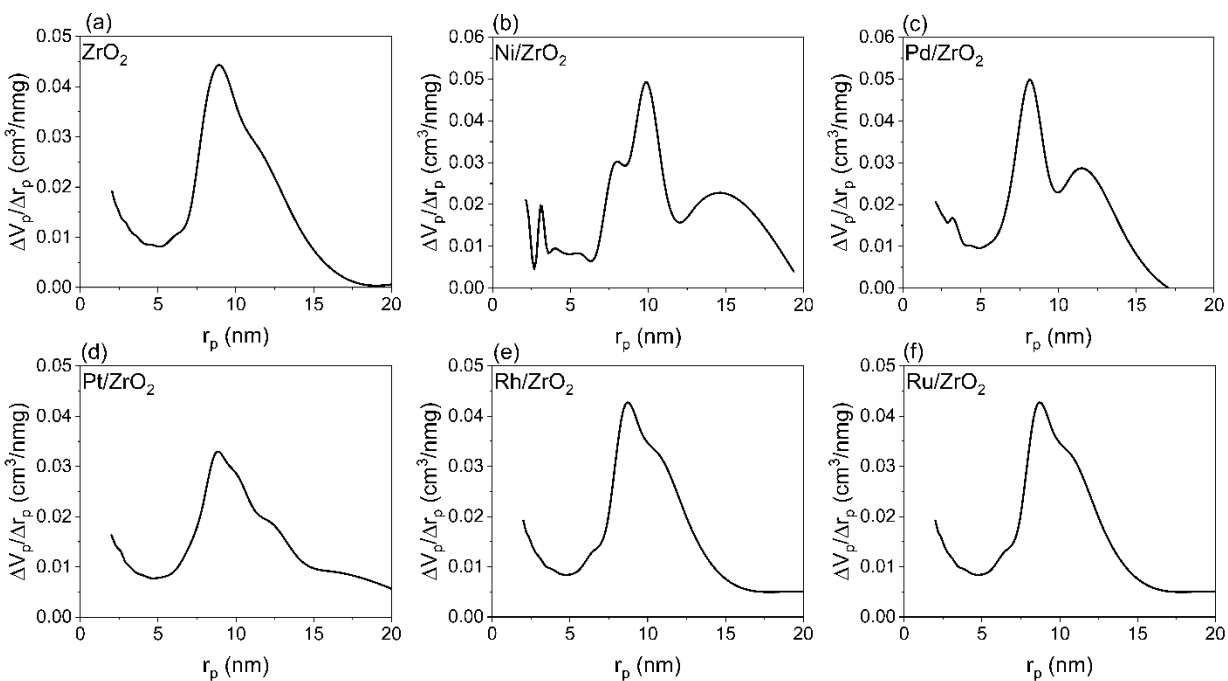


Figure S2. BJH pore size distribution of (a) the bare ZrO₂ support and the calcined (b) Ni/ZrO₂, (c) Pd/ZrO₂, (d) Pt/ZrO₂, (e) Rh/ZrO₂ and (f) Ru/ZrO₂ catalysts.

X-ray Diffraction

The X-ray diffractograms of the calcined catalysts are presented in Figure S3.

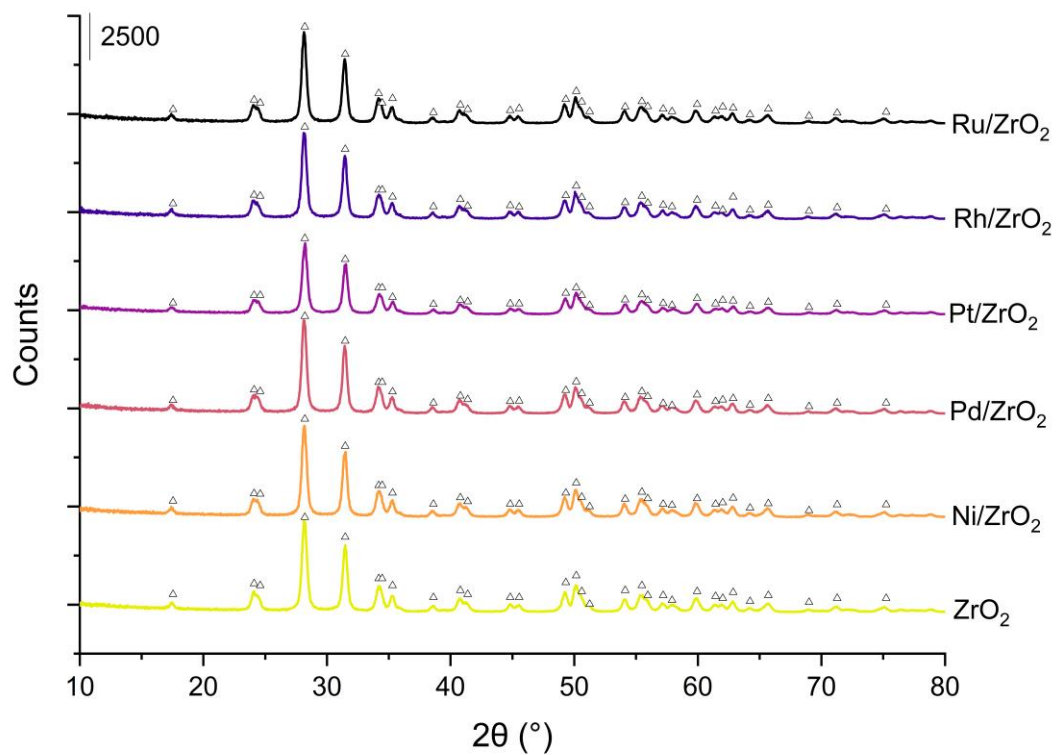


Figure S3. X-ray diffractograms of the calcined catalysts and the bare ZrO₂ support. The marked reflections (Δ) correspond to monoclinic ZrO₂ (ICDD 04-004-4339).

Scanning Transmission Electron Microscopy

A selection of representative STEM images of the calcined catalysts, with corresponding elemental EDS mappings, is presented in Figure S4.

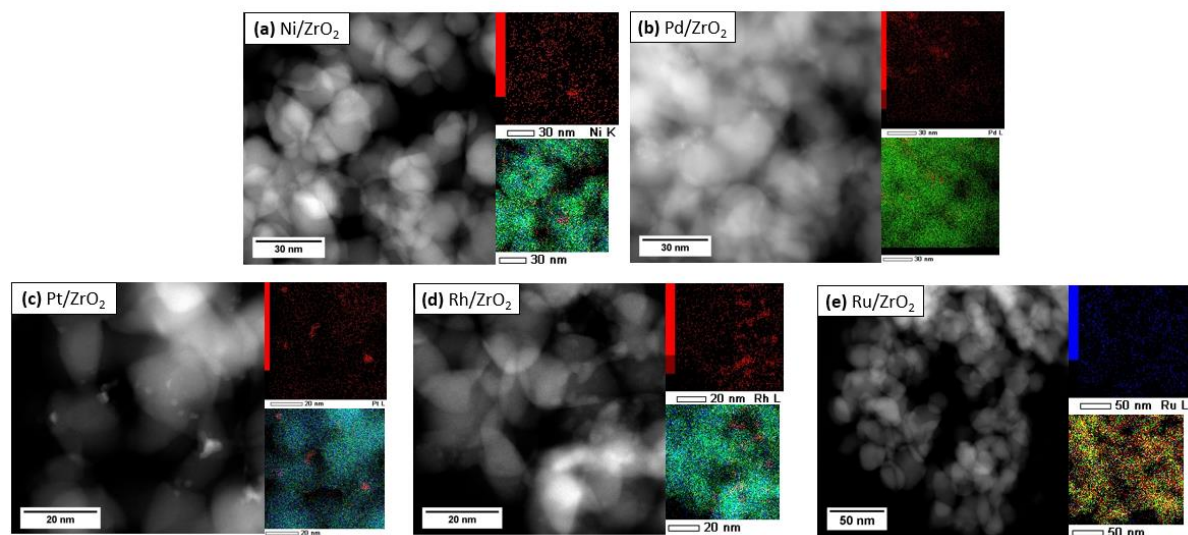


Figure S4. Representative STEM images and corresponding EDS mappings of the calcined (a) Ni/ZrO₂, (b) Pd/ZrO₂, (c) Pt/ZrO₂, (d) Rh/ZrO₂ and (e) Ru/ZrO₂ catalysts.

Table S1 presents the mean particle size and standard deviation of the mean particle size for the Pt/ZrO₂ and Rh/ZrO₂ catalysts, derived from STEM images. The particle size could not be reliably estimated from STEM images of the Ru/ZrO₂, Pd/ZrO₂ and Ni/ZrO₂ catalysts, due to an insufficient contrast between the active metal and the support.

Table S1. The mean metal particle size of the calcined Pt and Rh catalysts, derived from STEM images

Catalyst	$d_{m, \text{STEM}}$ (nm)	Standard deviation, $d_{m, \text{STEM}}$ (nm)
Pt/ZrO ₂	2.1	0.9
Rh/ZrO ₂	2.1	0.4

X-ray Photoelectron Spectroscopy

The XPS survey spectra of the samples are presented in Figure S5. The samples were reduced ex situ at 350 °C in H₂ before the measurements and transferred to the equipment in atmosphere.

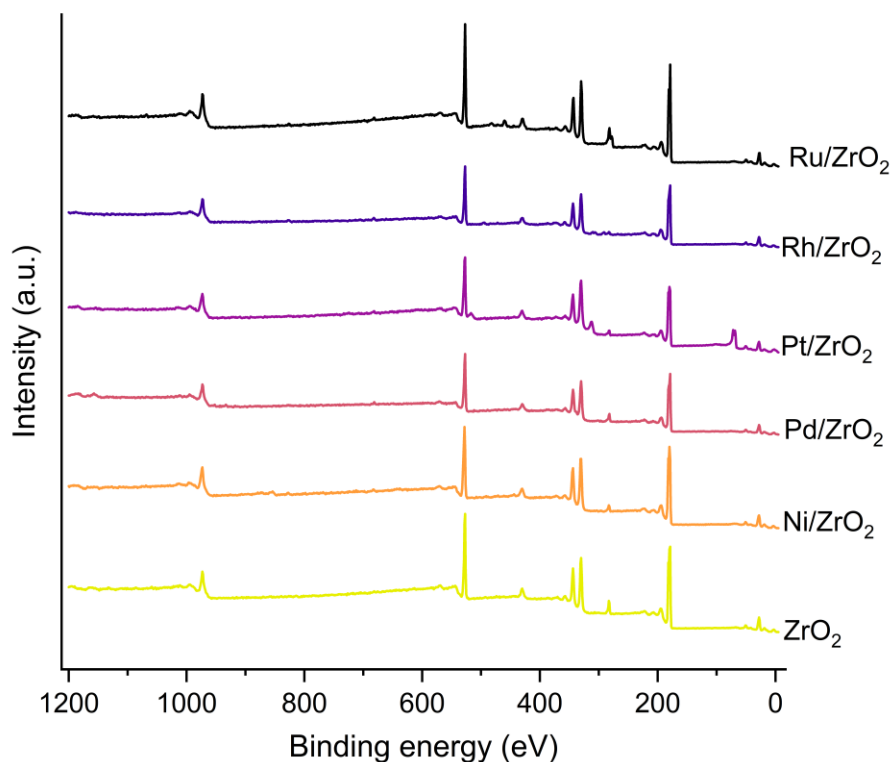


Figure S5. XPS survey spectra of the catalysts and the ZrO₂ support. The samples were reduced ex situ at 350 °C in H₂ before the measurements and transferred to the equipment in atmosphere.

The catalysts exhibited differences in the oxidation state of the ZrO₂ support and in the Zr 3d and O 1s binding energies, both relative to each other and to the bare ZrO₂. Table S2 presents the relative amounts of Zr in ZrO₂ and in a higher binding energy state. The higher binding energy component of Zr is herein referred to as the mixed state Zr oxide. Figure S6a displays the high resolution X-ray photoelectron spectra of the Zr 3d region for all catalysts and the ZrO₂ support, while the O 1s region is presented in Figure S6b.

Table S2. Relative amounts of Zr as ZrO₂ and in the mixed state Zr oxide, based on the XPS measurements

Catalyst ^a	ZrO ₂ (%)	Zr, mixed (%)
ZrO ₂	96	6
Ni/ZrO ₂	78	22
Pd/ZrO ₂	87	13
Pt/ZrO ₂	84	16
Rh/ZrO ₂	85	15
Ru/ZrO ₂	88	12

^aThe samples were reduced ex situ in H₂ at 350 °C before the XPS measurements and transferred to the equipment in atmosphere.

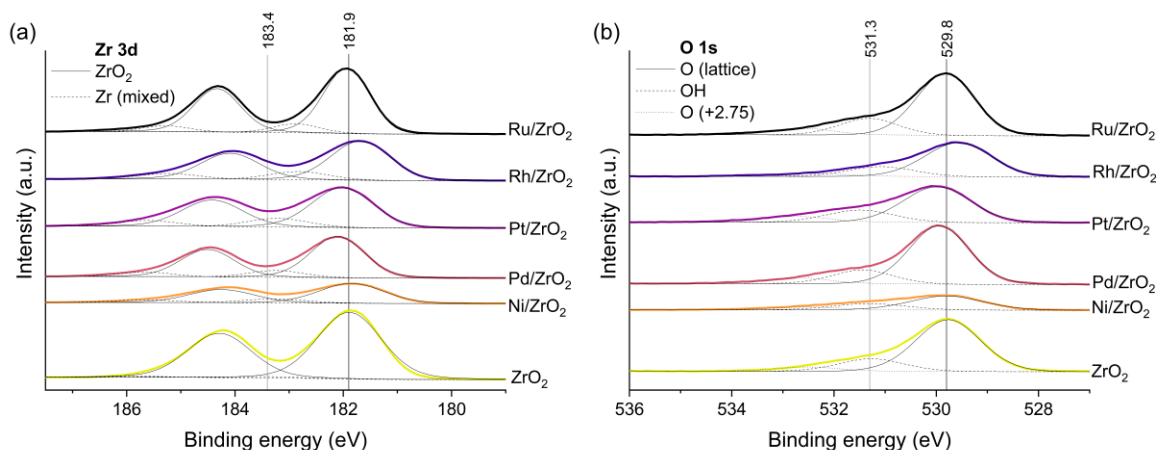


Figure S6. High resolution X-ray photoelectron spectra of the (a) Zr 3d and (b) O 1s regions. The binding energy of the main components of the bare ZrO₂ support have been indicated with vertical lines. The samples were reduced ex situ in H₂ at 350 °C before the XPS measurements and transferred to the equipment in atmosphere.

The Zr 3d and O 1s binding energies of the ZrO₂ support, Ru/ZrO₂ and Ni/ZrO₂ were similar (Figure S6). Meanwhile, the Zr 3d and O 1s binding energies of Pt/ZrO₂ and Pd/ZrO₂ were similar to each other and approximately 0.2 eV higher compared to the ZrO₂ support, suggesting that Pt and Pd may have withdrawn some electron density from the ZrO₂. Rh/ZrO₂ displayed approximately 0.3 eV lower Zr 3d and O 1s binding energies compared to the bare ZrO₂. Electron transfer from Rh to ZrO₂ may therefore have occurred, but it is also possible that the K present on the surface of Rh/ZrO₂ caused the shift. As seen from Table S2, the amount of the mixed state Zr oxide was considerably lower on the bare support (6.2%) compared to the catalysts (11.5-21.8%). The mixed state Zr oxide may be related to surface defects and to Zr bound to hydroxyl groups (Figure S6). Out of the catalysts, Ni/ZrO₂ had the highest relative amount of ZrO₂ in the mixed oxide state. The Zr 3d and O 1s binding energy shifts did not correlate with the relative amounts of Zr in the mixed oxide state in the samples.